Geophysical Journal International

*Geophys. J. Int.* (2022) **230,** 623–642
Advance Access publication 2022 February 23
GJI Seismology

https://doi.org/10.1093/gji/ggac074

# The effects of discontinuity topography in the mantle transition zone on global geodynamic observables and mantle heterogeneity

Petar Glišović,[1,2,3] Stephen P. Grand,[1] Chang Lu,[1] Alessandro M. Forte[4] and S. Shawn Wei[5]

[1] *Department of Geological Sciences, Jackson School of Geosciences, University of Texas at Austin, Austin , TX* 78712, *USA E-mail: pglisovic@gmail.com*
[2] *Department of Geological Sciences and Geological Engineering, Queen's University, Kingston, ON* K7L 3N6, *Canada*
[3] *GEOTOP, Université du Québec à Montréal, Montreal, QC H2L 2C4, Canada*
[4] *Department of Geological Sciences, College of Liberal Arts and Sciences, University of Florida, Gainesville, FL* 32611-2120, *USA*
[5] *Department of Earth and Environmental Sciences, College of Natural Science, Michigan State University, East Lansing, MI* 48824, *USA*

Accepted 2022 February 16. Received 2022 February 14; in original form 2021 July 15

## SUMMARY

Despite progress in tomographic imaging of Earth's interior, a number of critical questions regarding the large-scale structure and dynamics of the mantle remain outstanding. One of those questions is the impact of phase-boundary undulations on global imaging of mantle heterogeneity and on geodynamic (i.e. convection-related) observables. To address this issue, we developed a joint seismic-geodynamic-mineral physical tomographic inversion procedure that incorporates lateral variations in the depths of the 410- and 660-km discontinuities. This inversion includes *S*-wave traveltimes, SS precursors that are sensitive to transition-zone topography, geodynamic observables/data (free-air gravity, dynamic surface topography, horizontal divergence of tectonic plates and excess core-mantle boundary ellipticity) and mineral physical constraints on thermal heterogeneity. Compared to joint tomography models that do not include data sensitivity to phase-boundary undulations in the transition zone, the inclusion of 410- and 660-km topography strongly influences the inference of volumetric anomalies in a depth interval that encompasses the transition zone and mid-mantle. It is notable that joint tomography inversions, which include constraints on transition-zone discontinuity topography by seismic and geodynamic data, yield more pronounced density anomalies associated with subduction zones and hotspots. We also find that the inclusion of 410- and 660-km topography may improve the fit to the geodynamic observables, depending on the weights applied to seismic and geodynamic data in the inversions. As a consequence, we find that the amplitude of non-thermal density anomalies required to explain the geodynamic data decreases in most of the mantle. These findings underline the sensitivity of the joint inversions to the inclusion of transition-zone complexity (e.g. phase-boundary topography) and the implications for the inferred non-thermal density anomalies in these depth regions. Finally, we underline that our inferences of 410- and 660-km topography avoid a commonly employed approximation that represents the contribution of volumetric heterogeneity to *SS*-wave precursor data. Our results suggest that this previously employed correction, based on *a priori* estimates of upper-mantle heterogeneity, might be a significant source of error in estimating the 410- and 660-km topography.

**Key words:** Composition and structure of the mantle; Phase transitions; Joint inversion; Seismic tomography; Hotspots.

## 1 INTRODUCTION

Global seismic tomography remains our most powerful tool for mapping the structure of Earth's interior. However, despite great progress in methodology and first-order agreement among tomography models (e.g. Simmons *et al.* 2010; Ritsema *et al.* 2011; French & Romanowicz 2014; Moulik & Ekström 2016), there is still no consensus on the nature of the mantle structure (e.g. Ishii & Tromp 1999; Forte & Mitrovica 2001; Trampert *et al.* 2004; Garnero & McNamara 2008; Schuberth *et al.* 2009; Koelemeijer *et al.* 2017; Lau *et al.* 2017). This is due to intrinsic insensitivity of much seismic data to density (e.g. Cerveny 2001; Fichtner & Trampert 2011) which leads to

non-uniqueness in the interpretation of seismic velocities in terms of density variations. Constraining mantle density variations as well as seismic velocities places greater constraints on the thermochemical composition of the planet. Geodynamic observations (e.g. tectonic plate motions, gravity field and dynamic topography) are one means of providing important constraints on the density heterogeneity in the mantle.

Beginning with the work of Hager *et al.* (1985), *a posteriori* scaling of seismic tomography anomalies to density anomalies has been used to predict geodynamic observables. A seismic-velocity-to-density conversion factor based on experimental and theoretical results from mineral physics, which is often simplified in terms of a single constant scaling value, is a common approach for estimating density anomalies in the mantle (e.g. Conrad & Behn 2010; Ghosh *et al.* 2010). Alternatively, some studies carry out simultaneous inversions of global geodynamic data to determine an optimal velocity-to-density scaling factor that may be spatially variable (e.g. Hager & Clayton 1989; Corrieu *et al.* 1994; Panasyuk & Hager 2000; Forte & Mitrovica 2001). In most studies, the scaling of seismic velocity to density assumes that temperature has a dominant control on mantle heterogeneity. Furthermore, this scaling requires that relevant mineralogical variables and amplitudes of seismic velocity anomalies are well constrained (Forte *et al.* 2015). Satisfying all these requirements remains a great challenge. For example, Forte *et al.* (2015) showed that the average amplitude of the relative perturbations of seismic shear velocity derived from different tomography models has significant differences in the transition zone region and in the lowermost mantle (i.e. D"-layer).

Although numerous studies (e.g. Ghosh *et al.* 2010; Yang & Gurnis 2016) report fitting the geoid using *a posteriori* scaling of seismic tomography models to density, Forte *et al.* (2015) showed that this simple conversion does not provide a good fit to a full suite of available geodynamic observables (discussed below). They found that about 50 per cent of the power (i.e. mean square amplitude) in geodynamic data cannot be explained by *a posteriori* scaling of independently derived seismic tomography models. A more robust hypothesis test of the viability of a simple linear relation between velocity and density, and thus a mantle model dominated by thermal heterogeneity, is via simultaneous inversion of global seismic and geodynamic data that directly incorporate a mineral–physical relation between density and seismic velocity perturbations (Forte *et al.* 1994; Forte & Woodward 1997; Simmons *et al.* 2007, 2009, 2010). This joint seismic-geodynamic mapping of density anomalies involves a nonlinear coupling of the seismic velocity heterogeneity and the density–velocity scaling factor and hence requires an iterative approach. In this regard, Simmons *et al.* (2009, 2010) developed a nonlinear procedure for inferring a conversion factor that varied in 3-D (i.e. with depth and laterally at any given depth). The departure of the 3-D scaling relative to a 1-D scaling interprets as non-thermal (i.e. 'compositional/chemical') contributions to mantle heterogeneity. Lu *et al.* (2020) tested the sensitivity of this approach to different assumed viscosity models for the mantle and showed that in all cases substantial chemical heterogeneity was required to obtain sufficiently good fits to all geodynamic surface data.

The previous joint tomography inversions (e.g. Simmons *et al.* 2007, 2009, 2010; Lu *et al.* 2020) did not consider a potentially important source of density heterogeneity in the mantle arising from undulations in upper-mantle discontinuities near 410- and 660-km depth. The seismic data used in past inversions consisted of transmitted waves that are relatively insensitive to discontinuity topography. However, the geodynamic data, especially the gravity and dynamic surface topography, might be sensitive to upper-mantle discontinuity topography (e.g. Forte & Woodward 1997; Le Stunff & Ricard 1997). For example, Christensen (1998) suggested that phase boundary topography might help in reducing the misfit between modelled dynamic surface topography and the upper limit that 'observations' pose on its amplitude. Upper-mantle discontinuity topography has been determined locally using receiver functions (e.g. Lawrence & Shearer 2006; Dahm *et al.* 2017) and globally using underside reflections of shear waves that appear as precursors to the SS phase (e.g. Flanagan & Shearer 1998; Gu *et al.* 2003; Chambers *et al.* 2005; Schmerr & Garnero 2007; Houser *et al.* 2008; Deuss 2009). Although discontinuity topography is uncertain in detail, these studies find long-wavelength variations in depth of the 410- and 660-km discontinuities in the range of $\pm 20$ km (e.g. Flanagan & Shearer 1998; Gu *et al.* 2003; Lawrence & Shearer 2006; Schmerr & Garnero 2006; Houser *et al.* 2008). Variations of this magnitude may have a significant effect on the geodynamic observables (e.g. Forte & Woodward 1997) and thus call into question the conclusions of Lu *et al.* (2020) and Simmons *et al.* (2007, 2009, 2010).

In this study, we follow the approach of Simmons *et al.* (2010) and Lu *et al.* (2020) to jointly invert seismic and geodynamic data, but we also include transition-zone discontinuity topography as model parameters. To provide seismic constraints on the discontinuity topography, we add SS precursor data (Wei & Shearer 2017; Wei *et al.* 2020) to the inversion. The goal of this study is to examine the effects of topography on transition-zone discontinuities on volumetric mantle heterogeneity and on geodynamic surface observables.

## 2 DATA AND METHOD

We followed the method, first introduced by Simmons *et al.* (2009) and recently modified by Lu *et al.* (2020), to jointly invert seismic and geodynamic data. We have added 410- and 660-km discontinuity topography to the inversion as well as additional seismic and geodynamic data sets sensitive to discontinuity topography. Below we discuss the data sets used, followed by a discussion of the inversion method. As described in Lu *et al.* (2020), we first attempt to fit the data assuming that mantle heterogeneities

have a thermal origin. In a subsequent iteration, we invert the data for a total density model that has both thermal and non-thermal origins.

### 2.1. Geodynamic data

Here, we only provide a brief review of the geodynamic data used in our inversion as details are given in Lu *et al.* (2020). The geodynamic observations we used include: Earth's free-air gravity field, present-day horizontal divergence of tectonic plates, dynamic surface topography–all expanded up to spherical harmonic degree $L = 32$ and excess core–mantle boundary (CMB) ellipticity represented by a single degree-2 zonal harmonic. The free-air gravity field was derived from GRACE satellite data (Tapley *et al.* 2007). The rate of horizontal divergence of tectonic plate velocities was obtained from the GEODVEL model in the no-net-rotation frame of reference (Argus *et al.* 2010). The dynamic surface topography was inferred by removing all isostatic crustal contributions to Earth's observed surface topography (Forte & Perry 2000). The crustal corrections for dynamic surface topography are based on model ETOPO1 (Amante & Eakins 2009) and CRUST1.0 (Laske *et al.* 2013). The excess CMB ellipticity was inferred from studies of the Earth's free-core nutation (Mathews *et al.* 2002). We quantified the difference between the geodynamic data and model predictions in terms of variance reduction for $L = 32$ defined by the following formulae:

$$\mathrm{VR} = \left[1 - \frac{\sum_l \sum_{m=-l}^{+l} \left(\overline{O-P}\right)_l^m (O-P)_l^m}{\sum_l \sum_{m=-l}^{+l} \overline{O_l^m} O_l^m}\right] \times 100\%, \tag{1}$$

where $O$ and $P$ are the complex harmonic coefficients of the observed and predicted fields, respectively, and $\bar{}$ ('overline') denotes complex conjugation.

### 2.2. Seismic data

We use the same shear wave traveltime data as in Lu *et al.* (2020), consisting of (1) ∼70 000 hand-picked global S, ScS, SKS and SKKS phase traveltimes, as well as their surface bounce equivalents (SS, S3, S4, ScS2 and ScS3) and their upgoing wave equivalents (sS, sSS, sS3, sS4, sScS2 and sScS3); and (2) ∼226 000 traveltime measurements of horizontally polarized S, SS, SSS, ScS and ScSScS waves, which turn in the lower mantle, discussed in Lai *et al.* (2019). Traveltime residuals were computed with respect to a 1-D velocity model presented in Grand (1994) corrected for topography and crustal thickness using the CRUST1.0 model (Laske *et al.* 2013).

Underside *S*-wave reflections from upper-mantle discontinuities (SS precursors or SdS data) have been used to map mantle discontinuity topography on a global scale (e.g. Flanagan & Shearer 1998; Chambers *et al.* 2005). The SS precursor signals are usually weak on individual seismograms. To enhance the signals, stacking is typically employed. Here, we use SS precursor data from Wei *et al.* (2020) using two different stacking geometries: (1) caps spaced 5° apart with data stacked over a radius of 5° (5° × 5°) that are grouped in the following epicentral (source–receiver) distance ranges: 100–130°, 130–160° and 150–180°; and (2) caps spaced 5° apart with data stacked over a radius of 10° (5° × 10°) and using the entire epicentral distance range from 100° to 176°. SS precursors are stacked in the time domain along the theoretical SdS traveltime curve predicted by the IASP91 model (Kennett & Engdahl 1991). Details of the stacking method are given in Wei & Shearer (2017).

The stacks are aligned on the SS wave so that the SdS times in the stack are with respect to SS. We used a multichannel cross-correlation approach (Vandecar & Crosson 1990) to extract traveltimes from each of the 5° × 5° and 5° × 10° SS precursors separately. We first stacked all (normalized) SdS data after aligning them to their maximum amplitudes. Next, individual stacks with less than a 50 per cent correlation with the overall stacks were discarded and the process was repeated using a 60 per cent level of confidence. Once a reference stack was obtained (Fig. 1a), we correlated the original stacks with the reference stack to extract an SS-SdS time. We first use the 5° × 5° binned data to select all stacks from different distance ranges that have a good correlation with the reference stack, discarding stacks with a correlation lower than 90 per cent. We repeat this process using 5° × 10° bins for regions that did not have a 90 per cent correlation stack using the 5° × 5° binned data. For regions that did not have a 90 per cent correlation stack, we reduce the confidence limit to 80 per cent and repeat the procedure, first, for a 5° × 5° bin, and then, for a 5° × 10° bin.

We converted the SS-SdS times to residuals relative to predictions made using our starting *S*-wave model where a negative residual implies a relatively early SdS wave. For the SS waves, corrections were made for topography and crustal variations averaged for the area surrounding each cap using crustal model CRUST1.0 (Laske *et al.* 2013). The discontinuities were assumed to be at 410- and 660-km depth. The predicted times were computed using ray theory and the mid-distance appropriate for each stack. Fig. 1(b) shows the global distribution of SS-SdS (henceforth abbreviated by SdS) residuals used in this study after correction. Note the correlation of positive SdS times with cratons and negative SdS times with young oceans. This correlation indicates that the dominant signal in the SdS times comes from velocity variations in the shallow mantle.

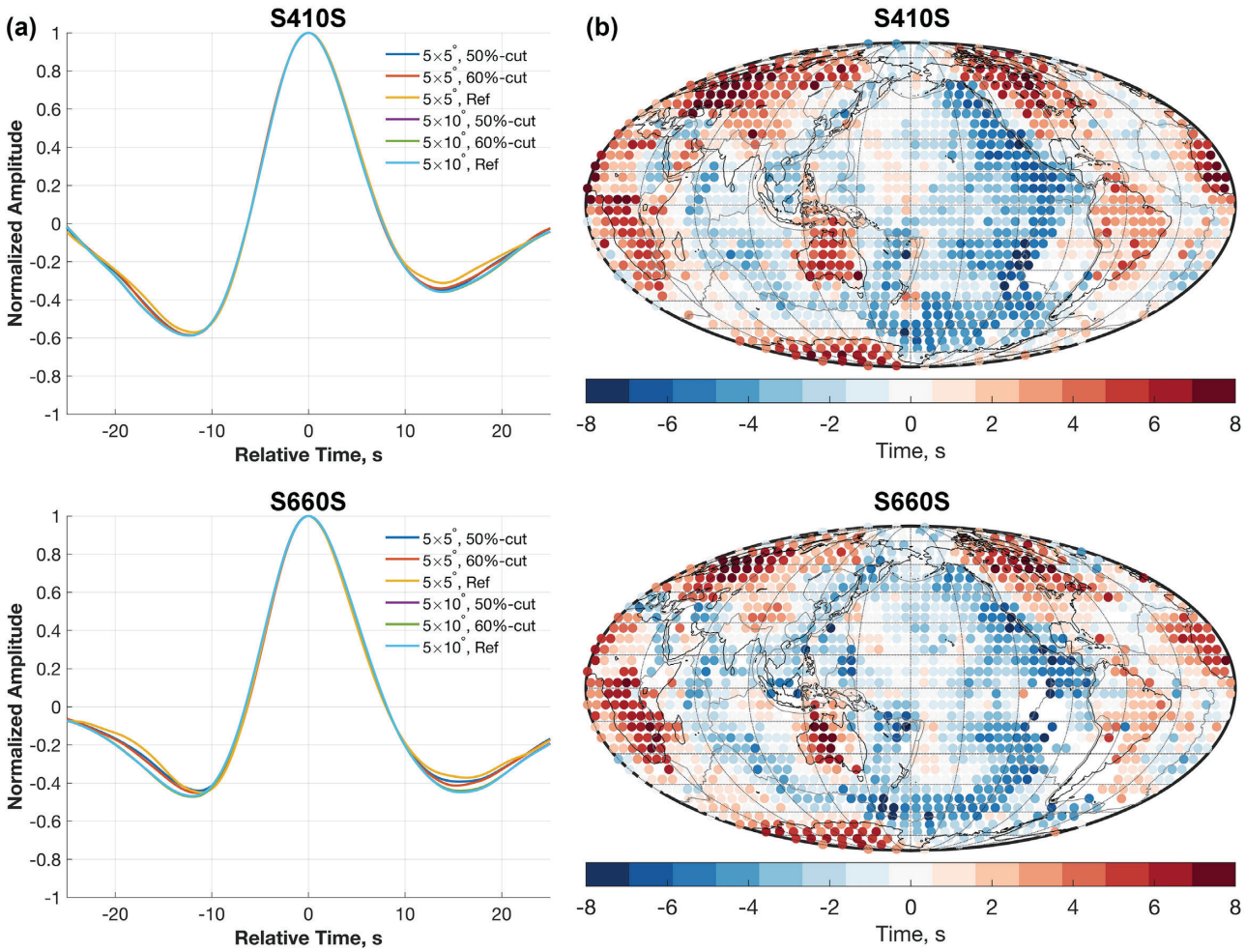


**Figure 1.** SdS data based on Wei & Shearer (2017) and Wei *et al.* (2020). (a) The reference stacks for S410S and S660S data. The reference time is the predicted SdS traveltime based on the IASP91 model (Kennett & Engdahl 1991). (b) The corrected traveltimes for S410S and S660S used in this study.

### 2.3. Inversion

To jointly invert seismic and geodynamic data, we require a linear relation between seismic shear velocity and density heterogeneities that can be represented by the following scaling factor, $R_{\rho/V_S}$:

$$R_{\rho/V_S} = \frac{\mathrm{d}\ln\rho}{\mathrm{d}\ln V_S}\,. \tag{2}$$

We adopt a depth-dependent scaling factor taken from Lu *et al.* (2020), which was obtained by extrapolating mineral physics measurements for a given chemical composition along a mantle geotherm, including both anharmonic and anelastic contributions (Karato & Karki 2001). This scaling factor was optimized for best fits to the seismic and geodynamic data within the error bars of the mineral physics measurements used. As described in Lu *et al.* (2020), it was found that fitting the geodynamic data required the use of a different scaling factor for cratonic lithosphere (from the surface to 250-km depth).

Following Simmons *et al.* (2009), we parametrized the mantle by a set of blocks approximately 275 $\times$ 275 km in lateral direction while the radial dimension varies from 75 to 240 km with thicker blocks in the lowermost mantle. We parametrize topography on the 410- and 660-km discontinuities using a spherical harmonic representation to degree and order 16. Given a relation between seismic velocity and density (eq. 2), the seismic and geodynamic data can be linearly related to the model in the following way:

$$\begin{bmatrix} L_S & A & P_S \\ \lambda_G G\left(R_{\rho/V_S}, -V_S\right) & 0 & \lambda_G \tilde{G}\left(R_{\rho/V_S}, -V_S\right) \\ \lambda_C C\left(R_{\rho/V_S}, -V_S\right) & 0 & \lambda_C \tilde{C}\left(R_{\rho/V_S}, -V_S\right) \\ \lambda_F F & 0 & 0 \\ \lambda_{SdS} L_{SdS} & 0 & \lambda_{SdS} P_{SdS} \end{bmatrix} \begin{bmatrix} \Delta m \\ \Delta q \\ \Delta r \end{bmatrix} = \begin{bmatrix} r_S \\ \lambda_G g \\ \lambda_C c \\ 0 \\ \lambda_{SdS} r_{SdS} \end{bmatrix}, \tag{3}$$

where $L_S$, $A$ and $P_S$ are the sensitivity kernels for the shear-wave traveltimes with respect to perturbations in slowness ($\Delta m$), earthquake location ($\Delta q$) and topography on the upper-mantle discontinuities ($\Delta r$), respectively. $r_S$ are the shear-wave traveltime residuals. $G$ and $C$ represent submatrices containing spatial representations of viscous-flow sensitivity kernels for the free-air gravity, dynamic surface topography and horizontal divergence of tectonic plates ($g$), and the excess ellipticity of CMB ($c$), respectively. Matrix $F$ is a second-order digital smoothing filter with 76 per cent of the weight applied to the lateral blocks and 24 per cent of the weight applied in the radial direction (Lu *et al.* 2020). $L_{\mathrm{SdS}}$ and $P_{\mathrm{SdS}}$ are the sensitivity kernels for the SdS data ($r_{\mathrm{SdS}}$) with respect to $\Delta m$ and $\Delta r$. All 'tilde'~variables represent the geodynamic sensitivity to phase undulations in the transition zone. The $\lambda$ terms are weighting factors that weight different observations in the inversion. We used the LSQR method (Paige & Saunders 1982) to solve eq. (3) for a number of inversions using different weighting factors as discussed below.

### 2.4. Seismic kernels

Both the *S*-wave times as well as the SdS data are sensitive to the volumetric heterogeneity in the mantle as well as undulations on the discontinuities. The volumetric kernels were computed using ray theory and consist of path lengths through the blocks. The SdS data are stacks that sample a finite area at the surface and the discontinuities. We ray-traced from a grid associated with the stacking area and averaged the resulting kernels. For each point on the grid, we ray-traced in four perpendicular azimuths—north, east, south and west—using the appropriate ray parameter for the stack. This was done for the SS waves as well as the underside reflected waves (SdS). For a particular SS-SdS kernel, the SS kernels were subtracted from the SdS kernels.

The procedure for the sensitivity of seismic data to discontinuity topography in the transition zone may be found in Appendix A.

### 2.5. Geodynamic kernels

The geodynamic kernels are mathematical representations of the linear (horizontal-wavelength-dependent) relation between surface observables and lateral density variations through the mantle (see eq. B2). The kernels are calculated assuming a compressible and gravitationally consistent mantle (see Forte *et al.* 2015 for detailed derivations). These kernels also account for the mechanical feedback on mantle flow arising from the plate-like character of the surface boundary that is mathematically expressed by a linear combination of free-slip and no-slip boundary conditions (Forte & Peltier 1994). The spherical harmonic representation of the geodynamic sensitivity kernels have been integrated onto the spatial block representation of mantle heterogeneity as in Simmons *et al.* (2009).

The procedure for the sensitivity of geodynamic data to topography on internal discontinuities may be found in Appendix B.

### 2.6. Viscosity profiles and density jumps

As discussed in Lu *et al.* (2020), the choice of mantle viscosity model represents a fundamental source of uncertainty in the joint tomographic inversions because the geodynamic kernels depend on the viscosity. In this study, we considered two mantle viscosity profiles: V1 (Mitrovica & Forte 2004) and V2 (Forte *et al.* 2010), both inferred from joint inversions of global convection-related observables and data associated with glacial isostatic adjustment (specifically, the Fennoscandian relaxation spectrum and a set of decay times determined from the post-glacial sea level history in Hudson Bay and Sweden). Compared with the V1 profile, V2 has a thicker, higher-viscosity lithosphere, a low-viscosity asthenospheric layer that is displaced to greater depth (220 km), a higher-viscosity 660-km layer and a higher average viscosity in the bottom half of the mantle (Fig. 2).

Another source of uncertainty constraining the effect of discontinuity topography on geodynamic data is the density jump at discontinuities (Shearer & Flanagan 1999). The PREM model has density jumps of 5.1 per cent at 400-km depth and 9.7 per cent at 670-km depth (Dziewonski & Anderson 1980). In contrast, Shearer & Flanagan (1999) found discontinuity density jumps of 1 per cent at 410-km depth and 5.6 per cent at 660-km depth with large error bars. The latter value also accords with the range of 660-km density jumps recently inferred by Lau & Romanowicz (2021). We therefore tested density jumps varying from 0 to 5.1 per cent and from 0 to 9.7 per cent for the 410-km and 660-km boundaries, respectively.

### 2.7. Non-thermal inversion

As noted above, we refer to models derived from an inversion of eq. (3) as 'thermal', although we also use a laterally variable velocity-to-density scaling for continental lithosphere to model the first-order effect of chemically distinct cratonic keels (Lu *et al.* 2020). To estimate outstanding non-thermal effects, we follow Lu *et al.* (2020) by fixing the velocity model as well as the discontinuity topography from the preceding thermal inversions and invert only for a 3-D scaling factor between seismic velocity and density:

$$\begin{bmatrix} \lambda_G G\,(\Delta m) \\ \lambda_C C\,(\Delta m) \\ \lambda'_F F \end{bmatrix} \Delta\, R^{\mathrm{3D}}_{\rho/V_{\mathrm{s}}} = \begin{bmatrix} \lambda_G \left(g - \tilde{G}\,(\Delta r)\right) \\ \lambda_C \left(c - \tilde{C}\,(\Delta r)\right) \\ 0 \end{bmatrix} . \tag{4}$$

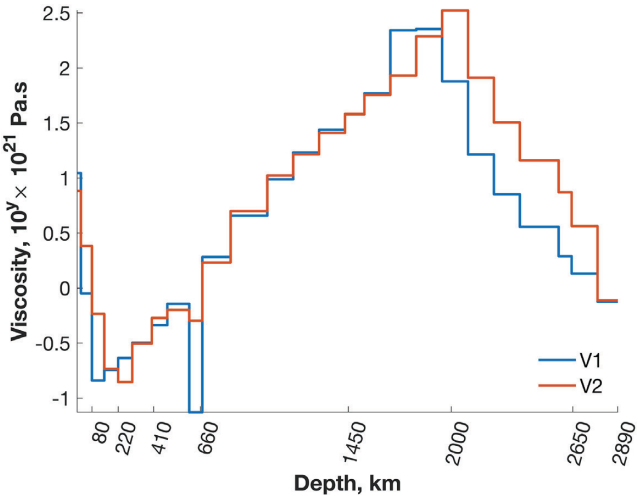


**Figure 2.** Viscosity models as a function of depth: V1 (Mitrovica & Forte 2004) and V2 (Forte *et al.* 2010).

**Table 1.** Code names for tomography models.

| Code Name | | Model Description |
|---|---|---|
| **Prefix** | **Suffixes** | |
| S | | Inversion that includes the S traveltimes only |
| SdS | | Inversion that includes both the S and SdS traveltimes |
| | V1 | Joint inversion that includes the sensitivity of geodynamic data to the V1 viscosity model |
| | V2 | Joint inversion that includes the sensitivity of geodynamic data to the V2 viscosity model |
| | ZERO | Inversion that includes S and SdS data only (i.e. no sensitivity to geodynamic data) |
| | PREM | Joint inversion that includes the sensitivity to the PREM density jumps |
| | 2 | Joint inversion with a decreased weight for the SdS data, $\lambda_{SdS} = 2$ (otherwise $\lambda_{SdS} = 3$) |
| | * | Joint inversion with an increased weight for the geodynamic data, $\lambda_G = 850$ (otherwise $\lambda_G = 650$) |

The density models obtained using the derived 3-D scaling factors are 'total density' models since they include both thermal and non-thermal contributions required to reconcile the seismic and geodynamic data. The smoothing weight $\lambda'_F$ is determined through an iterative process to make the roughness of the total density model the same as the corresponding thermal density model. The roughness of a density model is defined as the 2-norm of the regularized density model, that is $\|F(\Delta\rho)\|_2$ (Simmons 2007). Furthermore, the difference between the total density and thermal density models gives the non-thermal contributions to the mantle density anomalies.

## 3 RESULTS

We first perform the joint tomography inversions that do not include the SdS data set (henceforth denoted as the S models). These models (Lu *et al.* 2020) represent 'reference' ones used for the comparison versus models that include the data sensitivity to the 410- and 660-km discontinuity topography (henceforth denoted as the SdS models). As explained above, we consider two mantle viscosity profiles (V1 and V2). In the next step, we determine an optimal weight for the SdS data inverting only seismic data (henceforth denoted as the SdS-ZERO models). Using such optimal weight for the SdS data, we perform joint inversions that include the effect of 410- and 660-km discontinuities on both seismic and geodynamic data. Considering the uncertainties in density jumps across discontinuities, we test different combinations for these parameters. As a reference SdS model, we chose one with the PREM density jumps. We also quantify the separate contributions to SdS data fits by volumetric heterogeneity and transition-zone topography on discontinuities. We next consider the uncertainties in the SdS data and some of geodynamic data (particularly, the dynamic surface topography) by adjusting corresponding weights. All these models derive 'thermal' density anomalies. At the end, we invert for 3-D variations in the scaling factor of velocity to density obtaining the 'total' density anomalies. Table 1 summarize the code names of tomography models used in this study.

**Table 2.** Variance reductions.

| Data | 3-D | Models (per cent) | | | | | | |
|---|---|---|---|---|---|---|---|---|
| | | S | | SdS-ZERO | SdS-PREM $\lambda_{SdS} = 3$ | | SdS-PREM $\lambda_{SdS} = 2$ | |
| | | V2 | V1 | | V2 | V1 | V2 | V1 |
| Seismic | | 94.30 | 94.29 | 94.37 | 94.31 | 94.31 | 94.33 | 94.32 |
| | | | | | | | *94.30** | *94.30** |
| Gravity[a] | Thermal | 51.7 | 55.9 | | 50.4 | 53.6 | 56.0 | 61.3 |
| | | | | | | | *65.8** | *70.7** |
| | Total | 90.1 | 92.7 | | | | *92.7** | *94.7** |
| Topography[a] | Thermal | 61.6 | 62.9 | | 62.4 | 64.4 | 65.4 | 67.4 |
| | | | | | | | *68.6** | *70.3** |
| | Total | 79.7 | 80.0 | | | | *80.2** | *80.6** |
| Divergence[a] | Thermal | 81.1 | 81.0 | | 79.1 | 76.8 | 80.6 | 78.4 |
| | | | | | | | *87.5** | *86.1** |
| | Total | 99.5 | 99.6 | | | | *97.5** | *96.4** |
| CMB ellipticity[b] | Thermal | 97.7 | 98.5 | | 97.5 | 98.5 | 97.5 | 98.5 |
| | | | | | | | *96.9** | *98.1** |
| | Total | 99.5 | 99.4 | | | | *99.5** | *99.3** |
| SdS | | | | 86.7 | 84.8 | 84.6 | 80.9 | 80.4 |
| | | | | | | | *79.0** | *78.5** |
| S410S | | | | 88.0 | 86.9 | 86.9 | | |
| S660S | | | | 85.5 | 82.6 | 82.1 | | |

[a]The variance reductions for geodynamic data are calculated using $L = 32$.
[b]CMB excess ellipticity is in percentage relative error: $(1 - |(O - P)/O|) \times 100\%$, where $O$ and $P$ are observed and predicted values.
* Models with an increased weight for the geodynamic data ( $\lambda_G = 850$).

### 3.1. Effects of the 410- and 660-km discontinuity topography on data fits

#### *3.1.1. A reference joint tomography model that excludes the data sensitivity to the 410- and 660-km discontinuity topography (S model)*

The selection of different weights applied to multiple data sets is one of the difficulties inherent in joint tomography inversions because different weights will result in different models. We require weights for smoothing, $\lambda_F$, SdS data, $\lambda_{SdS}$, and the geodynamic data, $\lambda_G$ and $\lambda_C$ (eq. 3). Lu *et al.* (2020) demonstrated that 'optimal' values for $\lambda_F$, $\lambda_G$ and $\lambda_C$ are 2600, 650 and 2000, respectively, which we adopt here for the subsequent inversions. Employing this set of weights and the V2 viscosity model (Fig. 2) in a joint tomography inversion that excludes discontinuity topography kernels delivers fits of 94.30, 51.7, 61.6, 81.1 and 97.7 per cent for the *S*-wave data, free-air gravity anomalies, dynamic surface topography, horizontal divergence of tectonic plates and excess CMB ellipticity, respectively (Table 2). These fits to geodynamic observables are obtained assuming a purely thermal origin for the mantle density anomalies.

#### *3.1.2. Weighting the SdS data*

To determine an optimal weight for the SdS data, we first conduct a series of inversions of seismic data only. We test $\lambda_{SdS}$ (i.e. the SdS weight) values from 1 to 20 with an increment of 1, showing that an inflection point for a trade-off curve between the *S*-wave and SdS data fits is located for $\lambda_{SdS} = 3$ (Fig. 3). This value of the SdS weight produces a fit of 86.7 per cent for the combined SdS data. The S410S fit is 88.0 per cent and the S660S fit is 85.5 per cent. The mean value of differences between data and predictions are 0.12 and 0.05 s for S410S and S660S, respectively (Fig. 4a), which compare with corresponding traveltime anomalies of several seconds (Fig. 4b). Furthermore, this seismic inversion (henceforth denoted as the SdS-ZERO model) delivers an *S*-wave data fit of 94.37 per cent.

#### *3.1.3. A joint tomography model that includes the data sensitivity to the 410- and 660-km discontinuity topography (SdS model)*

In the next step, we run full joint inversions that include the effect of 410- and 660-km discontinuities on both seismic and geodynamic data. We tested different combinations for density jumps across the phase boundaries in the transition zone given the uncertainty in these parameters. For all inversions, the density jump-dependent changes in fits to gravity, surface topography and horizontal plate divergence are small, around 2–3 per cent (Figs 5a–c). In addition, the surface topography fit improves nearly proportional to the 660-km density jump (Fig. 5b), while the gravity fit improves if the 410-km density jump is lower than ∼2 per cent and the 660-km density jump is between ∼1.9 and ∼7.8 per cent (Fig. 5a). Compared to the S models, the SdS can, therefore, improve the fit to dynamic surface topography and gravity by a couple of per cent. However, the fit for horizontal plate divergence decreases by increasing the 660-km density jumps and this decrease can be up to ∼2 per cent (Fig. 5c). The CMB ellipticity fit remains relatively unchanged (Fig. 5d).

For the density jumps in PREM, the SdS-V2 model, which assumes purely thermal heterogeneity, yields fits of 94.31, 50.4, 62.4, 79.1, 97.5 and 84.8 per cent to the *S*-wave, free-air gravity, dynamic surface topography, horizontal plate divergence, excess CMB ellipticity and

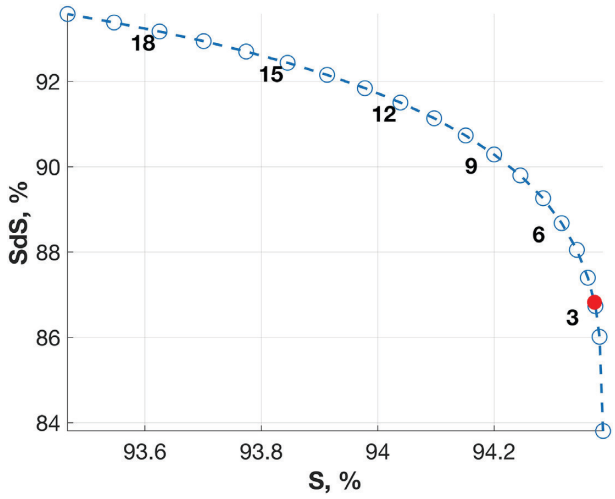


**Figure 3.** Trade-offs between *S*-wave and SdS data fits for a seismic inversion model (i.e. SdS-ZERO). The circles represent the SdS weights. The red circles show the inflection points for the inversion model.

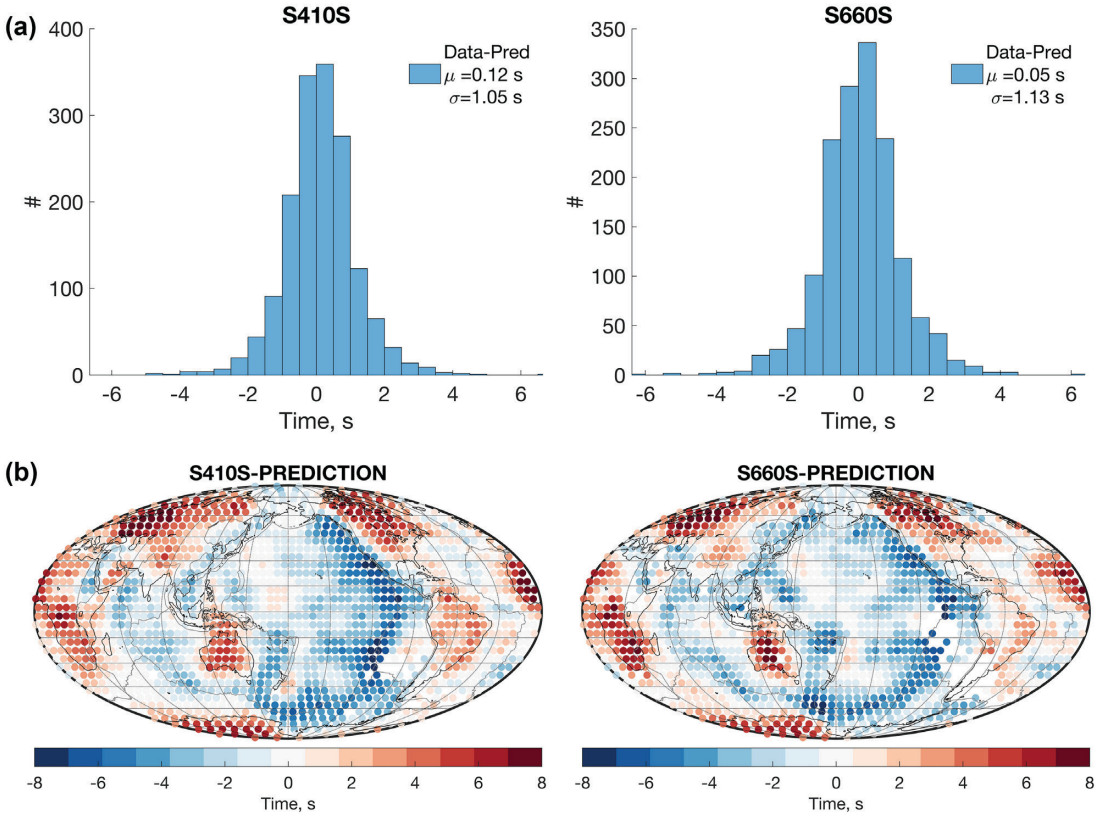


**Figure 4.** (a) Histograms of differences between SdS data (Fig. 1b) and SdS-ZERO model predictions (b).

SdS data, respectively (Table 2). The V1 thermal model delivers similar data fits; with an exception of the gravity fit that is ∼3 per cent higher compared to the V2 model (Table 2). Adding the geodynamic data and its sensitivity to the discontinuity topography slightly decreases the SdS fit for density jumps higher than ∼2 and ∼3 per cent across the 410- and 660-km phase boundary, respectively (Fig. 5e). For the PREM density jumps on discontinuities, the total fit to the combined SdS data is reduced by ∼2 per cent and is mostly due to changing the fit to the S660S data (Table 2). The *S*-wave data fit for the SdS-PREM models also slightly decreases (∼0.06 per cent) compared to the seismic (i.e. SdS-ZERO) inversions (Table 2).

We also quantify the separate contributions to SdS data fits by volumetric heterogeneity (not including discontinuity topography) and transition-zone topography on discontinuities. The inversions show the effect of volumetric heterogeneity on SS-precursor data is about three times larger (∼66 per cent) than that of the discontinuity topography (∼20 per cent) (Fig. 6). If density jumps on both discontinuities are increased, the volumetric contribution to fit increases by ∼2 per cent and the discontinuity topography contribution decreases by ∼5 per cent.

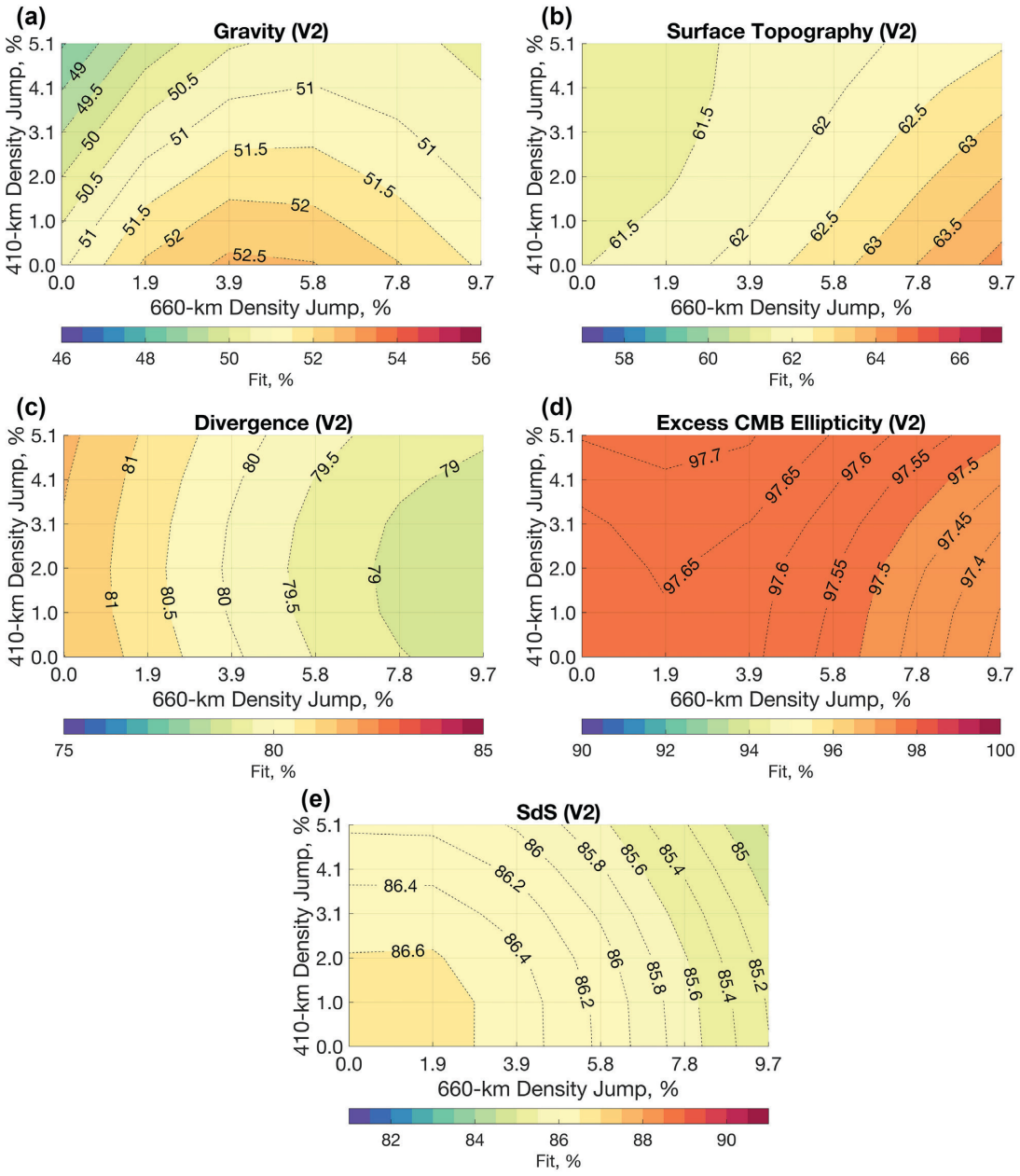


**Figure 5.** Data fits for the SdS-V2 models as a function of 410- and 660-km density jumps. (a) Free-air gravity; (b) dynamic surface topography; (c) horizontal divergence of tectonic plates; (d) excess ellipticity in the CMB; and (e) SdS.

The kernels for the SdS data are approximate since they represent an unknown distribution of rays in a stack. As such, it is not clear what uncertainties the SdS data have and how well they should be fit in an inversion. Inclusion of SdS data and boundary topography in our joint inversions did not degrade the fit to the geodynamic data but nor did it significantly improve the fits. To examine the potential of boundary topography to better fit the geodynamic data we reduce the SdS data weight from 3 to 2. Compared to the SdS-PREM models with $\lambda_{SdS} = 3$, the SdS-PREM models with $\lambda_{SdS} = 2$ (henceforth denoted as SdS-2-PREM models) improves fits for gravity, surface topography and horizontal plate divergence by about 7, 3 and 2 per cent, respectively (Table 2). The SdS fit decreases about 4 per cent, while the *S*-wave fit slightly increases. Given the increase in *S*-wave data fits, we increased the geodynamic data weight ($\lambda_G$) in an inversion that kept the same fit to *S*-wave data as the S inversion (i.e. 94.30 per cent). This exploration yields $\lambda_G = 850$. For the SdS-PREM models with $\lambda_{SdS} = 2$ and $\lambda_G = 850$ (henceforth denoted as SdS-2-PREM* models), we are able to further improve fits by ∼10, ∼3 and ∼7 per cent for the free-air gravity, dynamic surface topography and horizontal divergence of tectonic plates, respectively (Table 2). The SdS fit for the SdS-2-PREM* model is ∼79 per cent, which represents a decrease of 6 per cent compared to models employing the previous SdS weight: $\lambda_{SdS} = 3$ (Table 2).

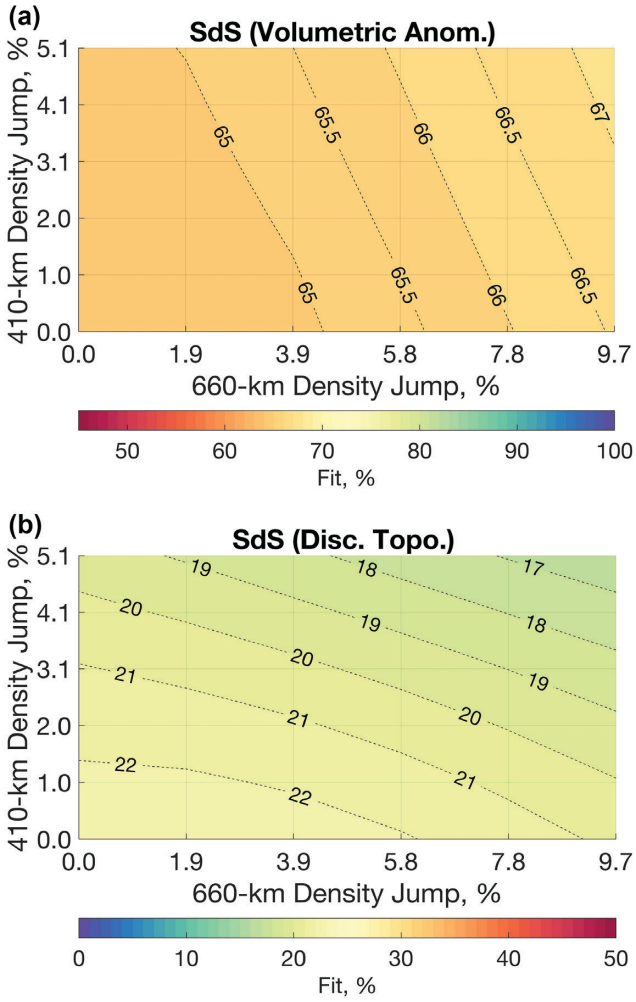


**Figure 6.** Density jump-dependent fits for SdS data due to SdS-V1 model inferences of volumetric variations (a) and discontinuity topography (b).

### 3.2. Effects of the 410- and 660-km discontinuity topography on inferences of volumetric anomalies

The inclusion of geodynamic data sensitivity to the 410- and 660-km discontinuity has a relatively high-impact on the inversion of volumetric anomalies inside the transition zone and adjacent layers (i.e. 325–425 km and 650–750 km). The differences in global thermal anomalies between joint tomographic inversions that do not include the effects of discontinuity topography in the transition zone (i.e. S models) and the SdS-2-PREM* models are highest in the layer between 525 and 650 km (Fig. 7a). Specifically, ∼12 and ∼20 per cent for the V2 and V1 models, respectively.

As discussed above, using the thermal models of density as starting models, we proceeded to invert for 3-D variations in the scaling factor of velocity to density to better fit the geodynamic data. We refer to the difference between these (i.e. total) density anomalies and those found using thermal mineral-physical constraints as 'non-thermal'. As in Simmons *et al.* (2006), we adjusted the smoothness weight to keep the roughness of the thermal and total density anomalies the same. In contrast to the thermal heterogeneity models, the inversions for non-thermal heterogeneity display much greater differences between S- and SdS-derived density anomalies. The differences for the PREM models that exceed ∼30 per cent are distributed between ∼425- and ∼1600-km depth with peak differences in layers 650–850 km (Fig. 7b). Furthermore, the SdS-2-PREM* models produce lower-amplitude of non-thermal heterogeneity in most of the mantle compared to the S models (Fig. 8).

The differences in the total density between S and SdS-2-PREM* models may range from ∼10 per cent to up to ∼35 per cent at depths that span Earth's interior from 250 to 1300 km (Fig. 7c).

As discussed above, the difference between models incorporating discontinuity topography and models that do not is largest between ∼400- and ∼1600-km depth. Therefore, we focus on density anomalies in three depth layers, in Figs 9–11 (525–650, 750–850 and 1300–1450 km), to provide a quantitative spatial assessment of the differences arising from the two inversion approaches (with and without data sensitivity to transition-zone topography). The complete catalogue of density maps (and their differences) is shown in the Supporting Information.

Compared to the S models, the maps of total density for the SdS-2-PREM* models at 525–650 km have stronger and more spatially coherent positive density anomalies associated with subduction under western Pacific (Figs 9i–l and Supporting Information Fig. S23).

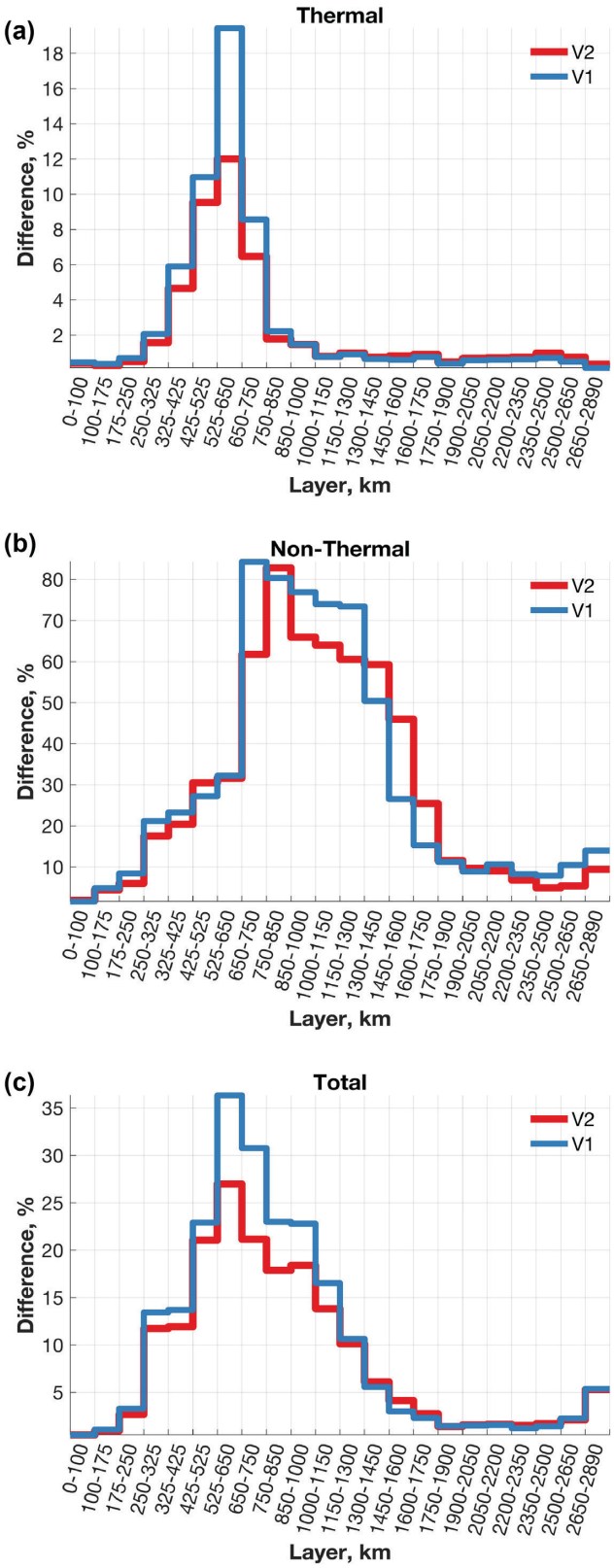


**Figure 7.** The differences between inversions as a function of depth layers. The differences for (a) thermal, (b) non-thermal and (c) total density models using the V1 and V2 viscosities. The differences are calculated in terms of 'the variance reduction', that is using the following formula: 100 per cent − VR(0,*P*), where VR(0,*P*) is given with eq. (1), and O: S-model and P: SdS-2-PREM* model.

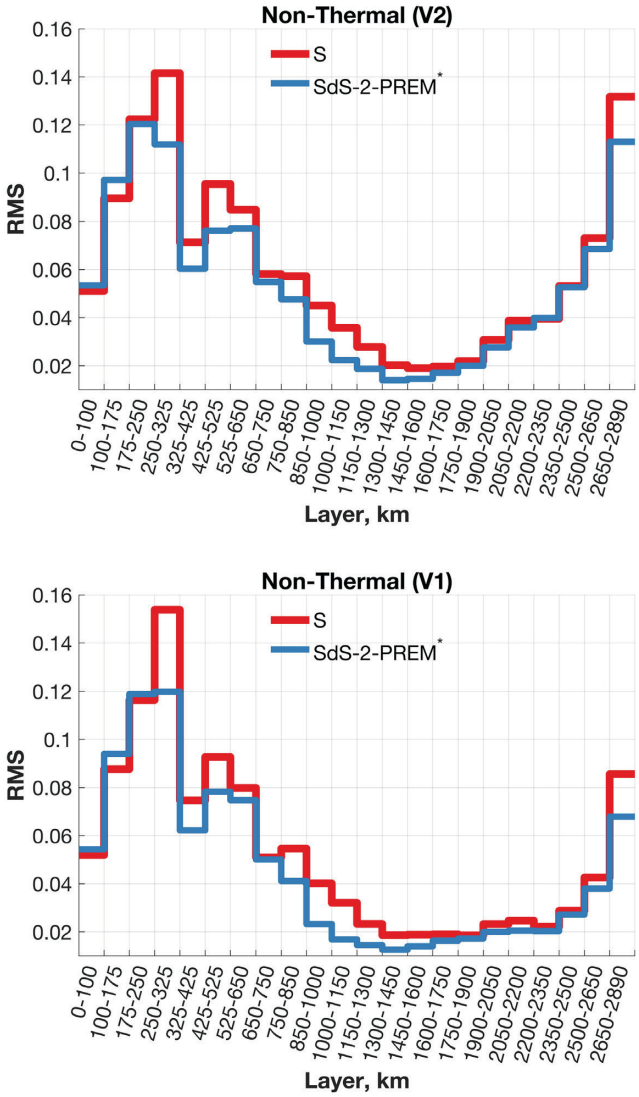


**Figure 8.** The RMS of non-thermal density anomalies as a function of depth layers.

Furthermore, the negative density perturbations derived from the SdS-2-PREM* models are also more coherent beneath the Pacific Plate, especially beneath the South Pacific. There are also stronger negative density anomalies beneath the Perm region, and Hoggar and Tibesti hotpots in Africa at these depths (Supporting Information Fig. S23). In contrast, the strong negative anomaly beneath the Indian Plate, which is characteristic of the S-models, is subdued by the inclusion of the discontinuity topography in the SdS inversions (Figs 9i–l).

Further comparison between S and SdS-2-PREM* inversions shows less non-thermal density anomalies resolved by the SdS models in the layer from 750 to 850 km (Figs 10e–h). In addition, the SdS inferences of non-thermal anomaly have an opposite sign in some regions associated with subduction zones. Consequently, the positive lateral variations in total density for the SdS-2-PREM* models are stronger beneath subduction zones (i.e. Farallon, South America, Indonesia, Tonga, Philippines, Scotia Plate; Figs 10i–l and Supporting Information Fig. S23). With further respect to the S-models in the layer from 750 to 850 km, the lateral variations in total density for the SdS-2-PREM* inversions also show: (1) more coherent negative anomalies beneath the South and East Pacific; (2) stronger negative anomaly beneath Comoros; and (3) the appearance of negative anomalies beneath the Darfur Volcanic Province/hotspot and Perm region (Figs 10i–l and Supporting Information Fig. S23).

Compared to the S-inversions, the SdS-2-PREM* models yield much weaker non-thermal density anomalies beneath eastern Africa between 1300 and 1450 km (Figs 11e–h). They also deliver a much stronger negative anomaly in the non-thermal density along the west coast of Africa (Cape Verde and Canary hotspots). Other notable differences between SdS-2-PREM* and S inversions in the layer from 1300 and 1450 km are a diminished positive anomaly of non-thermal density under the central Pacific and the absence of negative anomaly beneath the east coast of US in the SdS models (Figs 11e–h).

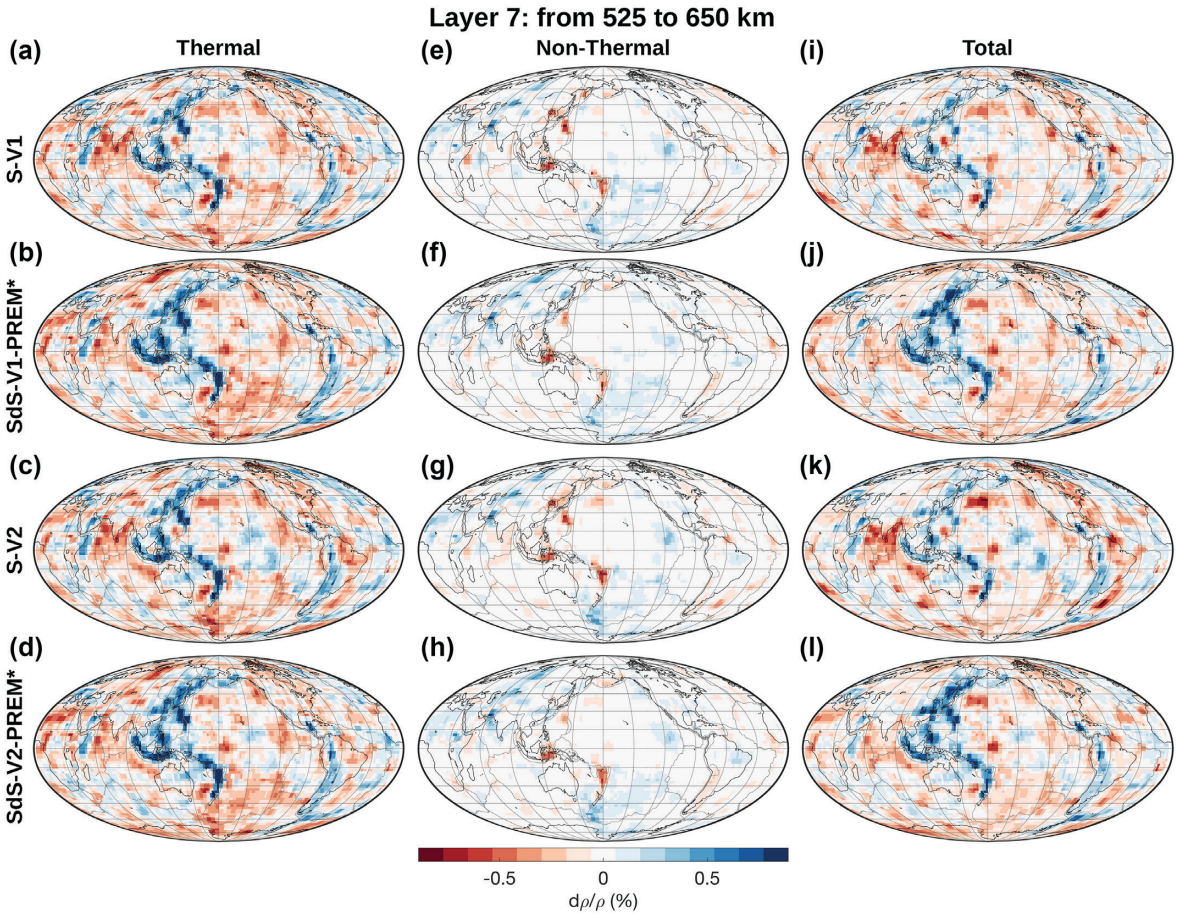


**Figure 9.** Lateral variations in density from 525 to 650 km derived from joint inversions. The row corresponds to the following models: (first) S-V1; (second) SdS-2-V1-PREM*; (third) S-V2; and (fourth) SdS-2-V2-PREM*. The column represents: (a–d) thermally induced density models obtained using the corrected 1-D optimal scaling factor; (e–h) the difference between the total and thermal density models, which is caused by non-thermal effects; (i–l) the total density derived by letting the scaling factor vary in 3-D to best fit the geodynamic data while keeping the velocity model fixed. The black and grey solid lines show the coastlines and plate boundaries, respectively.

### 3.3. The 410- and 660-km topography: lateral variations in mantle transition zone (MTZ) thickness

Lateral variations in mantle transition zone (MTZ) thickness are defined in terms of the difference between $\Delta r_{410}$ and $\Delta r_{660}$.The models reveal reduced MTZ thickness beneath the East Pacific Rise and many places under the Pacific Plate, while the greatest thickness is found under subduction zones in the western Pacific (Figs 12e and f). These inversions find thicker MTZ beneath the South-American, Indonesian, Mediterranean subduction systems as well as the Farallon slab and Scotia Plate. In contrast, the most thinned transition zone is found beneath (or in the vicinity of) hotspots such as the Perm, Hoggar, Afar, Comores, Crozet-Marion, Tasmania, San Felix, Yellowstone, Tristan, Fernando, Canary, Cape Verde, etc. (Figs 12e and f).

To quantify the impact of geodynamic data on the inference of discontinuity topography, we compare two SdS models: one that excludes (SdS-2-ZERO) and other that includes the geodynamic observations (SdS-2-V2-PREM *). The differences in discontinuity topography between SdS-2-ZERO and SdS-2-V2-PREM * models (Figs 12a–d) are ∼40 and ∼50 per cent for the 410- and 660-km phase boundaries, respectively. The discontinuity topography results for the V1-inversions are similar to the V2-ones. Namely, the difference between the SdS-2-V1-PREM* and SdS-2-V2-PREM* is ∼5 per cent for each of the discontinuities in the transition zone. Finally, adding geodynamic data in inversions decreases the global RMS amplitude of discontinuity topography inferences (Figs 12a–d).

## 4 DISCUSSIONS AND CONCLUSIONS

The sensitivity of dynamic surface topography and gravity to the 410- and 660-km discontinuities is directly proportional to the density jumps across these upper-mantle phase boundaries. Compared to joint tomography models that do not include the effect of 410- and 660-km topography (i.e. S models), the phase boundary topography in the transition zone may reduce the misfit between inversion predictions and observations for surface topography and gravity by a couple of percent. The improvement in fitting the surface topography agrees qualitatively with suggestions from other studies (e.g. Christensen 1998) and it is mostly due to the 660-km discontinuity. The improvement in fitting the gravity is more restrictive, preferring modest discontinuity density jumps as independently suggested by Shearer & Flanagan (1999) and Lau

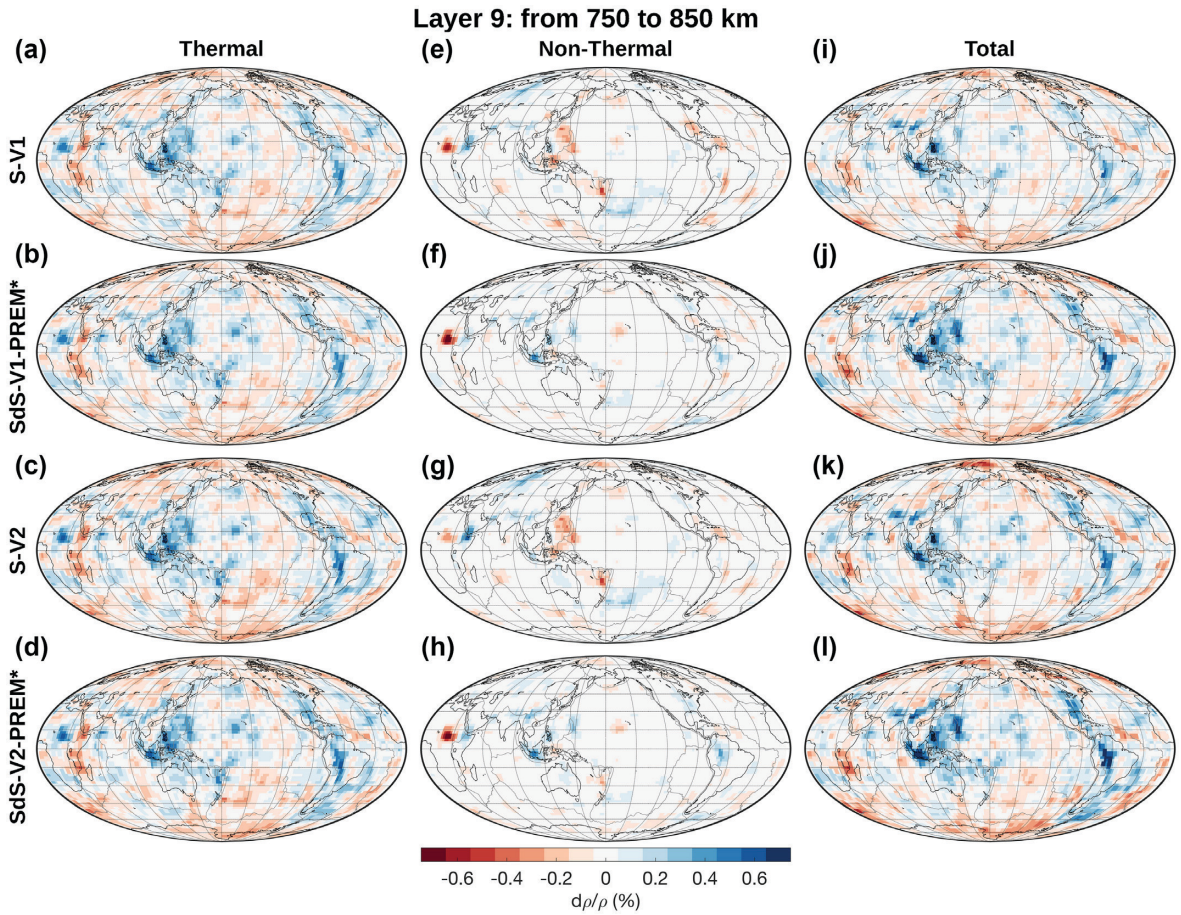


**Figure 10.** Lateral density variations between 750 and 850 km derived from joint inversions. The columns and rows are the same as in Fig. 9.

& Romanowicz (2021) (i.e. 1 per cent at 410 depth and 5.6 per cent at 660 km depth). We note, in particular, that the latter study (Lau & Romanowicz 2021) strongly indicates that the '660'-km density jump in PREM (actually located at 670 km) is situated at the upper limit of the acceptable values (5.1–8.2 per cent) revealed by a Backus-Gilbert inversion of normal-mode centre frequencies. Also, if we relax the weighting applied for the SdS data and modestly increase the weight for geodynamic data, then fits to the gravity, surface topography and divergence can increase by up to ∼14, ∼7 and ∼6 per cent, respectively, even for the larger amplitude (e.g. PREM) density jumps (Table 2).

The total density anomalies for the PREM-density jump model fit geodynamic data higher than 90 per cent, except for the surface topography whose fit is ∼80 per cent (Table 2). We note that this fit to dynamic topography has improved by about 10 per cent relative to that delivered by the GyPSuM joint tomography model (Simmons *et al.* 2010), in the same range of horizontal wavelengths. The latter model used an inference of dynamic topography obtained using a crustal correction based on CRUST2.0 (Bassin *et al.* 2000) rather than CRUST1.0 used here. Such differences, which highlight uncertainties in the 'observed' dynamic topography, point to future joint inversions employing a range of dynamic topography models obtained in independent studies (e.g. Hoggard *et al*. 2016).

The inclusion of geodynamic data sensitivity to discontinuity topography significantly affects the inference of 3-D volumetric heterogeneity in the mantle (Fig. 7). More importantly, the amplitude of non-thermal density anomalies, required to explain the geodynamic data, decreases in most of the mantle (Fig. 8). These findings point to the importance of resolving the trade-off between mantle buoyancy arising from discontinuity topography and volumetric heterogeneity. Therefore, the interpretations of density heterogeneity inferred from past global tomography models (especially between ∼250 and ∼1300 km) may be significantly biased if this trade-off is not accounted for.

Tomography models appear to generally underestimate the amplitude of seismic anomalies in subducting slabs, and thus density anomalies if one scales velocity to density (Zhan *et al*. 2014). Our results show the neglect of upper mantle discontinuity undulations in most global tomography inversions can be partly responsible for the discrepancy. Further comparison with the S models shows that the inclusion of data sensitivity to the 410- and 660-km discontinuities in joint tomographic inversions amplifies and resolves the total density perturbations associated with hotspots at depths that span the transition zone and mid-mantle. These properties of the SdS models are mostly due to significantly subdued non-thermal density anomalies that are generally required to more fully reconcile geodynamic data constraints. Furthermore, some of these non-thermal anomalies are found to be correlated with thermal anomalies, which was not the case for the S models, and thereby explains the highest difference between SdS and S models is for the non-thermal density anomaly.

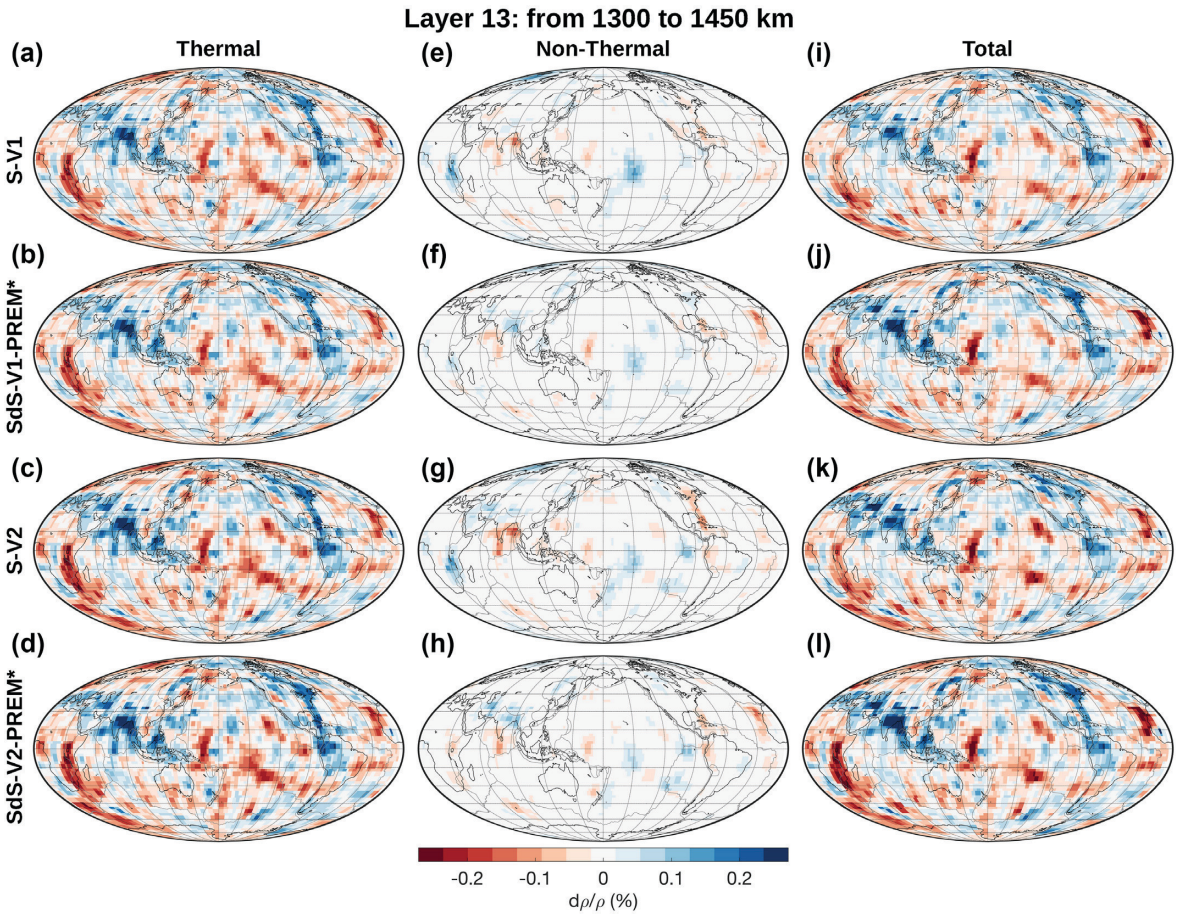


**Figure 11.** Lateral density variations between 1300 and 1450 km derived from joint inversions. The columns and rows are the same as in Fig. 9.

Previous joint tomography models (i.e. the S models, Simmons *et al*. 2010; Lu *et al*. 2020) showed that the 'central' parts of African and Pacific LLSVPs have positive non-thermal density anomalies in the lowermost mantle. These positive contributions to the total density anomalies can extend upwards from the D"-layer to mid-mantle depths (Lu *et al*. 2020). To some extent, our results differ from these findings. Specifically, the SdS models deliver a smaller amount of non-thermal density in the layer between 2650 and 2890 km compared to the joint tomography models that do not include the sensitivity of data to the 410- and 660-km topography (Fig. 8). This is partly due to relatively decreased amplitude of non-thermal density anomalies in the centres of African and Pacific LLSVPs (Supporting Information Fig. S22). Most importantly, the inclusion of data sensitivity to the 410- and 660-km topography cancels the need for positive non-thermal contributions to the total density anomalies beneath the location of LLSVPs, especially for the African, at depths between ∼1000 and ∼1600 km (Supporting Information).

While our study demonstrates the geodynamic importance of phase-boundary undulations in the transition zone and their impact on inferences of global mantle heterogeneity, it also provides direct maps of 410- and 660-km topography that range from -14 to 15 km and from -18 to 19 km, respectively. These results agree well with previous studies (e.g. Flanagan & Shearer 1998; Gu *et al*. 2003; Lawrence & Shearer 2006; Schmerr & Garnero 2006; Houser *et al*. 2008). We find that our inferred lateral variations in MTZ thickness reveal that thinner regions are well correlated to hotspot locations (Courtillot *et al*. 2003), while increased thickness of MTZ is correlated with major subduction zones (Fig. 12). These results support the classical interpretation of discontinuity topography in terms of equilibrium phase changes at 410- and 660-km depths, which are sensitive to ambient lateral variations in mantle temperature via the Clapeyron slope of the phase change (e.g. Forte & Woodward 1997). In this case, the transport of hot (less dense) material across the 410- and 660-km discontinuities causes a thinner MTZ, and the opposite for cold, more dense heterogeneity, because the Clapeyron slopes of the 410- and 660-km phase changes are of opposite signs (e.g. Bina & Helffrich 1994).

There are modelling approaches that jointly invert for mantle velocity and transition-zone discontinuity topographies (e.g. Moulik & Ekstrom 2014) but some of seismic inversions for discontinuity topography in the transition zone applied a correction for lateral heterogeneity in the upper mantle (e.g. Shearer & Masters 1992; Chambers *et al*. 2005; Houser & Williams 2010; Lee *et al*. 2014; Wang *et al*. 2017). This correction represents a source of uncertainties due to differences in inversion techniques and data. Using the joint tomography approach that includes the sensitivity of data to discontinuity topography in the transition zone, we avoid using such *a priori* corrections for lateral heterogeneity in the upper mantle. Our inversions for the 410- and 660-km topographies show that contributions of volumetric anomalies to

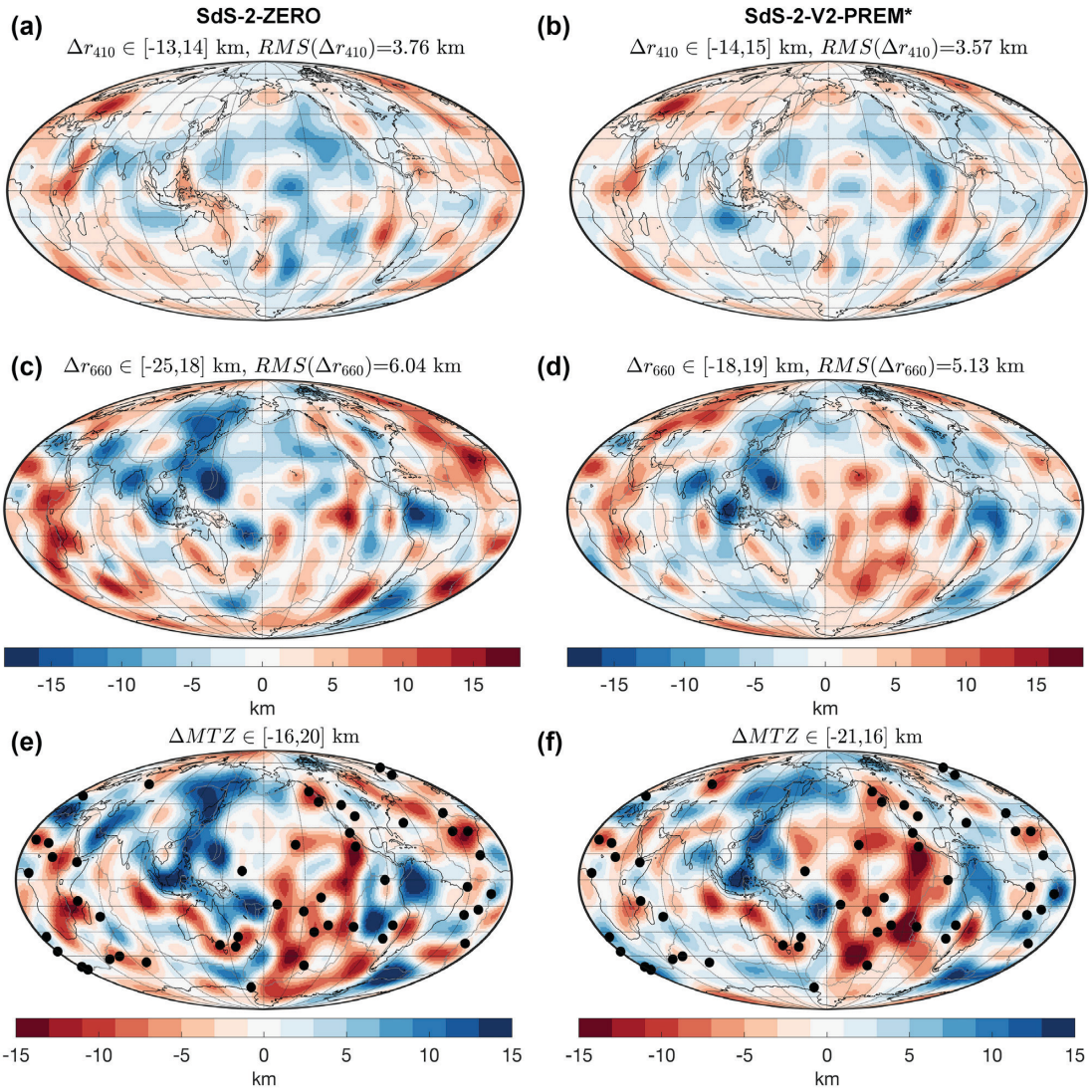


**Figure 12.** The phase boundary topography in the transition zone. The first and second columns show the SdS-2-ZERO and SdS-2-V2-PREM∗ inversion models, respectively. (a and b) Topography at 410 km; (c and d) topography at 660 km; (e and f) lateral variations in mantle transition zone (MTZ) thickness. The black and grey solid lines show the coastlines and plate boundaries, respectively. The black circles represent the location of present-day hotspots (Courtillot *et al.* 2003).

the SdS data are about three times higher than that of the discontinuity topography (Fig. 6). This implies that corrections for the upper-mantle lateral heterogeneity is a significant source of uncertainty, or error, in seismic inferences of topography on discontinuities.

## ACKNOWLEDGMENTS

This research was supported by the Jackson School of Geosciences at the University of Texas at Austin. PG acknowledges support for this work provided by Research Centre in Earth System Dynamics (GEOTOP), UQAM as well as Compute Canada. AMF acknowledges support for this work provided by NSF grant EAR-1903108 as well as by the University of Florida. AMF also acknowledges support from the French 'Programme d'investissements d'avenir' under the auspices of the GYPTIS project–ANR 19 MPGA 0007. SSW was supported by the MSU Geological Sciences Endowment. PG, SPG and AMF developed the scientific concepts and modelling techniques presented here and jointly wrote the paper. PG created the code, SS precursor kernels, corrected SS precursor data and figures. PG also run the inversions and performed the analysis of results. The *S*-wave data and kernels are provided by SPG and CL. CL also provided the joint inversion code, while the SSW provided the SS precursor data. AMF created he geodynamic kernels.

## DATA AVAILABILITY

The data underlying this paper will be shared on request to the corresponding author.

## REFERENCES


Amante, C. & Eakins, B.W., 2009. ETOPO1 1 arc-minute global relief model: procedures, data sources and analysis, in *NOAA Technical Memorandum NESDIS NGDC-24,* National Geophysical Data Center, NOAA.

Argus, D.F., Gordon, R.G., Heflin, M.B., Ma, C., Eanes, R.J., Willis, P., Peltier, W.R. & Owen, S.E., 2010. The angular velocities of the plates and the velocity of Earth's centre from space geodesy, *Geophys. J. Int.,* **180**(3), 913–960.

Bassin, C., Laske, G. & Masters, G., 2000. The current limits of resolution for surface wave tomography in North America, *EOS, Trans. Am. geophys. Un.,* **81,** F897.

Bina, C. R. & Helffrich, G., 1994. Phase transition Clapeyron slopes and transition zone seismic discontinuity topography, *J. geophys. Res.,* **99**(B8), 15 853–15 860.

Cerveny, V., 2001. *Seismic Ray Theory,* Cambridge Univ. Press.

Chambers, K., Woodhouse, J.H. & Deuss, A., 2005. Topography of the 410-km discontinuity from PP and SS precursors, *Earth Planet. Sci. Lett.,* **235**(3–4), 610–622.

Christensen, U.R., 1998. Dynamic phase boundary topography by latent heat effects, *Earth planet. Sci. Lett.,* **154,** 295–306.

Conrad, C.P. & Behn, M.D., 2010. Constraints on lithosphere net rotation and asthenospheric viscosity from global mantle flow models and seismic anisotropy, *Geochem. Geophys. Geosyst.,* **11,** Q05W05, doi:10.1029/2009GC002970.

Corrieu, V., Ricard, Y. & Froidevaux, C., 1994. Converting mantle tomography into mass anomalies to predict the Earth's radial viscosity, *Phys. Earth planet. Inter.,* **84**(1–4), 3–13.

Courtillot, V., Davaille, A., Besse, J. & Stock, J., 2003. Three distinct types of hotspots in the Earth's mantle, *Earth planet. Sci. Lett.,* **205**(3–4), 295–308.

Dahm, H.H., Gao, S.S., Kong, F. & Liu, K.H., 2017. Topography of the mantle transition zone discontinuities beneath Alaska and its geodynamic implications: constraints from receiver function stacking, *J. geophys. Res.,* **122**(12), 10 352–10 363.

Deuss, A., 2009. Global observations of mantle discontinuities using SS and PP precursors, *Surv. Geophys.,* **30**(4–5), 301–326.

Dziewonski, A.M. & Anderson, D.L., 1980. Preliminary reference Earth model, *Phys. Earth planet. Inter.,* **25**(4), 297–356.

Dziewonski, A.M. & Gilbert, F., 1976. The effect of small, aspherical perturbations on travel times and a re-examination of the corrections for ellipticity, *Geophys. J. R. astr. Soc.,* **44**(1), 7–17.

Fichtner, A. & Trampert, J., 2011. Hessian kernels of seismic data functionals based upon adjoint techniques, *Geophys. J. Int.,* **185,** 775–798.

Flanagan, M.P. & Shearer, P.M., 1998. Global mapping of topography on transition zone velocity discontinuities by stacking SS precursors, *J. geophys. Res.,* **103**(B2), 2673–2692.

Forte, A.M. & Mitrovica, J.X., 2001. Deep-mantle high-viscosity flow and thermochemical structure inferred from seismic and geodynamic data, *Nature,* **410,** 1049–1056.

, eds Forte, A.M., Peltier, W.R., Dmowska, R. & Saltzman, B., 1994. The kinematics and dynamics of poloidal–toroidal coupling in mantle flow: the importance of surface plates and lateral viscosity variations, in *Advances in Geophysics,* Vol. 36, pp. 1–119, Elsevier.

Forte, A.M. & Perry, H. C., 2000. Geodynamic evidence for a chemically depleted continental tectosphere, *Science,* **290**(5498), 1940–1944.

Forte, A.M., Quéré, S., Moucha, R., Simmons, N.A., Grand, S.P., Mitrovica, J.X. & Rowley, D.B., 2010. Joint seismic–geodynamic-mineral physical modelling of African geodynamics: a reconciliation of deep-mantle convection with surface geophysical constraints, *Earth planet. Sci. Lett.,* **295**(3–4), 329–341.

Forte, A.M., Simmons, N.A. & Grand, S.P., 2015. Constraints on 3-D seismic models from global geodynamic observables: implications for the global mantle convective flow, in *Treatise on Geophysics,* 2nd edn, Vol. 1, pp. 853–907, ed. Schubert, G., Elsevier.

Forte, A.M. & Woodward, R.L., 1997. Seismic-geodynamic constraints on three-dimensional structure, vertical flow, and heat transfer in the mantle, *J. geophys. Res.,* **102**(B8), 17 981–17 994.

French, S.W. & Romanowicz, B.A., 2014. Whole-mantle radially anisotropic shear velocity structure from spectral-element waveform tomography, *Geophys. J. Int.,* **199**(3), 1303–1327.

Garnero, E.J. & McNamara, A.K., 2008. Structure and dynamics of Earth's lower mantle, *Science,* **320**(5876), 626–628.

Ghosh, A., Becker, T.W. & Zhong, S.J., 2010. Effects of lateral viscosity variations on the geoid, *Geophys. Res. Lett.,* **37,** doi:10.1029/2009GL040426.

Grand, S.P., 1994. Mantle shear structure beneath the Americas and surrounding oceans, *J. geophys. Res.,* **99**(B6), 11 591–11 621.

Gu, Y.J., Dziewoński, A.M. & Ekström, G., 2003. Simultaneous inversion for mantle shear velocity and topography of transition zone discontinuities, *Geophys. J. Int.,* **154**(2), 559–583.

Hager, B.H. & Clayton, R.W., 1989. Constraints on the structure of mantle convection using seismic observations, flow models, and the geoid, in *Mantle Convection: Plate Tectonics and Global Dynamics,* Fluid Mechanics of Astrophysics and Geophysics, No. 4, pp. 657–763, Gordon and Breach Science Publishers.

Hager, B.H., Clayton, R.W., Richards, M.A., Comer, R.P. & Dziewonski, A.M., 1985. Lower mantle heterogeneity, dynamic topography and the geoid, *Nature,* **313**(6003), 541–545.

Hoggard, M.J., White, N. & Al-Attar, D., 2016. Global dynamic topography observations reveal limited influence of large-scale mantle flow, *Nat. Geosci.,* **9,** 456–463.

Houser, C., Masters, G., Flanagn, M. & Shearer, P., 2008. Determination and analysis of long-wavelength transition zone structure using SS precursors, *Geophys. J. Int.,* **174,** 178–194.

Houser, C. & Williams, Q. 2010. Reconciling Pacific 410 and 660 km discontinuity topography, transition zone shear velocity patterns, and mantle phase transitions, *Earth Planet. Sci. Lett.,* **296**(3-4),255–266.

Ishii, M. & Tromp, J., 1999. Normal-mode and free-air gravity constraints on lateral variations in velocity and density of Earth's mantle, *Science,* **285**(5431), 1231–1236.

Karato, S.I. & Karki, B.B., 2001. Origin of lateral variation of seismic wave velocities and density in the deep mantle, *J. geophys. Res.,* **106**(B10), 21 771–21 783.

Kennett, B.L.N. & Engdahl, E.R., 1991. Traveltimes for global earthquake location and phase identification, *Geophys. J. Int.,* **105**(2), 429–465.

Koelemeijer, P., Deuss, A. & Ritsema, J., 2017. Density structure of Earth's lowermost mantle from Stoneley mode splitting observations, *Nat. Commun.,* **8**(1), 1–10.

Lai, H., Garnero, E.J., Grand, S.P., Porritt, R.W. & Becker, T.W., 2019. Global travel time data set from adaptive empirical wavelet construction, *Geochem. Geophys. Geosyst.,* **20,** 2175–2198.

Laske, G., Masters, G., Ma, Z. & Pasyanos, M., 2013. Update on CRUST1.0—a 1-degree global model of Earth's crust, *Geophys. Res. Abstr.,* **15,** 2658.

Lau, H.C., Mitrovica, J.X., Davis, J.L., Tromp, J., Yang, H.Y. & Al-Attar, D., 2017. Tidal tomography constrains Earth's deep-mantle buoyancy, *Nature,* **551**(7680), 321–326.

Lau, H.C.P. & Romanowicz, B.(2021). Constraining jumps in density and elastic properties at the 660 km discontinuity using normal mode data via the Backus–Gilbert method, *Geophys. Res. Lett.,* **48,** e2020GL092217.

Lawrence, J.F. & Shearer, P.M., 2006. A global study of transition zone thickness using receiver functions, *J. geophys. Res.,* **111**(B6), doi:10.1029/2005JB003973.

Le Stunff, Y. & Ricard, Y., 1997. Partial advection of equidensity surfaces: a solution for the dynamic topography problem?, *J. geophys Res.,* **102,** 24 655–24 667.

Lee, S.H., Rhie, J., Park, Y. & Kim, K.H. 2014. Topography of the 410 and 660 km discontinuities beneath the Korean Peninsula and southwestern Japan using teleseismic receiver functions, *Journal of Geophysical Research: Solid Earth,* **119**(9),7245–7257.

Lu, C., Forte, A.M., Simmons, N.A., Grand, S.P., Kajan, M.N., Lai, H. & Garnero, E.J., 2020. The sensitivity of joint inversions of seismic and geodynamic data to mantle viscosity, *Geochem. Geophys. Geosyst.,* **21,** e2019GC008648.

Mathews, P.M., Herring, T.A. & Buffett, B.A., 2002. Modeling of nutation and precession: new nutation series for nonrigid Earth and insights into the Earth's interior, *J. geophys. Res.,* **107**(B4), ETG 3–1-ETG 3-26.

Mitrovica, J.X. & Forte, A.M. 2004. A new inference of mantle viscosity based upon joint inversion of convection and glacial isostatic adjustment data, *Earth planet. Sci. Lett.,* **225**(1–2), 177–189.

Moulik, P. & Ekström, G. 2014. An anisotropic shear velocity model of the Earth's mantle using normal modes, body waves, surface waves and long-period waveforms, *Geophys. J. Int.,* **199**(3), 1713–1738.

Moulik, P. & Ekström, G., 2016. The relationships between large-scale variations in shear velocity, density, and compressional velocity in the Earth's mantle, *J. geophys. Res.,* **121**(4), 2737–2771.

Paige, C.C. & Saunders, M.A., 1982. LSQR: an algorithm for sparse linear equations and sparse least squares, *ACM Trans. Math. Softw.,* **8**(1), 43–71.

Panasyuk, S.V. & Hager, B.H., 2000. Inversion for mantle viscosity profiles constrained by dynamic topography and the geoid, and their estimated errors, *Geophys. J. Int.,* **143**(3), 821–836.

Ritsema, J., Deuss, A., van Heijst, H.J. & Woodhouse, J. H., 2011. S40RTS: a degree-40 shear-velocity model for the mantle from new Rayleigh wave dispersion, teleseismic traveltime and normal-mode splitting function measurements, *Geophys. J. Int.,* **184**(3), 1223–1236.

Schmerr, N. & Garnero, E. J., 2007. Upper mantle discontinuity topography from thermal and chemical heterogeneity, *Science,* **318**(5850), 623–626.

Schmerr, N. & Garnero, E., 2006. Investigation of upper mantle discontinuity structure beneath the central Pacific using SS precursors, *J. geophys. Res.,* **111**(B8).

Schuberth, B.S.A., Bunge, H.-P. & Ritsema, J., 2009. Tomographic filtering of high-resolution mantle circulation models: can seismic heterogeneity be explained by temperature alone?, *Geochem. Geophys. Geosyst.,***10,** Q05W03, doi:10.1029/2009GC002401.

Shearer, P.M. & Flanagan, M.P., 1999, Seismic velocity and density jumps across the 410- and 660-kilometer discontinuities, *Science,* **285,** 1545–1548.

Shearer, P.M. & Masters, T.G. 1992. Global mapping of topography on the 660-km discontinuity, *Nature,* **355,** 791–796.

Simmons, N.A., 2007. Mantle heterogeneity and flow from seismic and geodynamic constraints, *PhD thesis*, University of Texas at Austin.

Simmons, N.A., Forte, A.M., Boschi, L. & Grand, S. P., 2010. GyPSuM: a joint tomographic model of mantle density and seismic wave speeds, *J. geophys. Res.,* **115**(B12), B12310.

Simmons, N.A., Forte, A.M. & Grand, S.P., 2006. Constraining mantle flow with seismic and geodynamic data: A joint approach, *Earth Planet. Sci. Lett.,* **246**(1-2), 109–124.

Simmons, N.A., Forte, A.M. & Grand, S.P., 2007. Thermochemical structure and dynamics of the African superplume, *Geophys. Res. Lett.,* **34**(2), doi:10.1029/2006GL028009.

Simmons, N.A., Forte, A.M. & Grand, S.P., 2009. Joint seismic, geodynamic and mineral physical constraints on three-dimensional mantle heterogeneity: Implications for the relative importance of thermal versus compositional heterogeneity, *Geophys. J. Int.,* **177**(3), 1284–1304.

Tapley, B., Ries, J., Bettadpur, S., Chambers, D., Cheng, M., Condi, F. & Poole, S., 2007. The GGM03 mean Earth gravity model from GRACE, in *The American Geophysical Union Fall Meeting,* American Geophysical Union, San Francisco, CA.

Trampert, J., Deschamps, F., Resovsky, J. & Yuen, D., 2004. Probabilistic tomography maps chemical heterogeneities throughout the lower mantle, *Science,* **306**(5697), 853–856.

VanDecar, J.C. & Crosson, R.S., 1990. Determination of teleseismic relative phase arrival times using multi-channel cross-correlation and least squares, *Bull. Seismol. Soc. Am.,* **80**(1), 150–169.

Wang, X., Li, J. & Chen, Q.-F. 2017. Topography of the 410 km and 660 km discontinuities beneath the Japan Sea and adjecent regions by analysis of multiple-ScS waves, *J. geophys. Res.: Solid Earth,* **122,** 1264–1283.

Wei, S.S. & Shearer, P.M., 2017. A sporadic low-velocity layer atop the 410 km discontinuity beneath the Pacific Ocean, *J. geophys. Res.,* **122,** 5144–5159.

Wei, S.S., Shearer, P.M., Lithgow-Bertelloni, C., Stixrude, L. & Tian, D., 2020. Oceanic plateau of the Hawaiian mantle plume head subducted to the uppermost lower mantle, *Science,* **370**(6519), 983–987.

Yang, T. & Gurnis, M., 2016. Dynamic topography, gravity and the role of lateral viscosity variations from inversion of global mantle flow, *Geophys. J. Int.,* **207**(2), 1186–1202.

Zhan, Z., Helmberger, D.V. & Li, D., 2014. Imaging subducted slab structure beneath the Sea of Okhotsk with teleseismic waveforms, *Phys. Earth planet. Inter.,* **232,** 30–35.

## SUPPORTING INFORMATION

Supplementary data are available at *GJI* online.

**Figure S1.** Lateral variations in density from 0 to 100 km derived from joint inversions. The row corresponds to the following models: (first) S-V1; (second) SdS-2-V1-PREM*; (thirrd) S-V2; and (fourth) SdS-2-V2-PREM*. The column represents: (a–d) thermally induced density models obtained using the corrected 1-D optimal scaling factor; (e–h) the difference between the total and thermal density models, which is caused by non-thermal effects; (i–l) the total density derived by letting the scaling factor vary in 3-D to best fit the geodynamic data while keeping the velocity model fixed. The black and grey solid lines show the coastlines and plate boundaries, respectively.

**Figure S2.** Lateral density variations between 100 and 175 km derived from joint inversions. The columns and rows are the same as in Fig. S1.

**Figure S3.** Lateral density variations between 175 and 250 km derived from joint inversions. The columns and rows are the same as in Fig. S1.

**Figure S4.** Lateral density variations between 250 and 325 km derived from joint inversions. The columns and rows are the same as in Fig. S1.

**Figure S5.** Lateral density variations between 325 and 425 km derived from joint inversions. The columns and rows are the same as in Fig. S1.

**Figure S6.** Lateral density variations between 425 and 525 km derived from joint inversions. The columns and rows are the same as in Fig. S1.

**Figure S7.** Lateral density variations between 525 and 650 km derived from joint inversions. The columns and rows are the same as in Fig. S1.

**Figure S8.** Lateral density variations between 650 and 750 km derived from joint inversions. The columns and rows are the same as in Fig. S1.
**Figure S9.** Lateral density variations between 750 and 850 km derived from joint inversions. The columns and rows are the same as in Fig. S1.
**Figure S10.** Lateral density variations between 850 and 1000 km derived from joint inversions. The columns and rows are the same as in Fig. S1.
**Figure S11.** Lateral density variations between 1000 and 1150 km derived from joint inversions. The columns and rows are the same as in Fig. S1.
**Figure S12.** Lateral density variations between 1150 and 1300 km derived from joint inversions. The columns and rows are the same as in Fig. S1.
**Figure S13.** Lateral density variations between 1300 and 1450 km derived from joint inversions. The columns and rows are the same as in Fig. S1.
**Figure S14.** Lateral density variations between 1450 and 1600 km derived from joint inversions. The columns and rows are the same as in Fig. S1.
**Figure S15.** Lateral density variations between 1600 and 1750 km derived from joint inversions. The columns and rows are the same as in Fig. S1.
**Figure S16.** Lateral density variations between 1750 and 1900 km derived from joint inversions. The columns and rows are the same as in Fig. S1.
**Figure S17.** Lateral density variations between 1900 and 2050 km derived from joint inversions. The columns and rows are the same as in Fig. S1.
**Figure S18.** Lateral density variations between 2050 and 2200 km derived from joint inversions. The columns and rows are the same as in Fig. S1.
**Figure S19.** Lateral density variations between 2200 and 2350 km derived from joint inversions. The columns and rows are the same as in Fig. S1.
**Figure S20.** Lateral density variations between 2350 and 2500 km derived from joint inversions. The columns and rows are the same as in Fig. S1.
**Figure S21.** Lateral density variations between 2500 and 2650 km derived from joint inversions. The columns and rows are the same as in Fig. S1.
**Figure S22.** Lateral density variations between 2650 and 2890 km derived from joint inversions. The columns and rows are the same as in Fig. S1.
**Figure S23.** Differences in lateral density variations between the SdS and S models. The columns represent the models inverted using different viscosity profiles. The rows represent the depth layers.
Please note: Oxford University Press is not responsible for the content or functionality of any supporting materials supplied by the authors. Any queries (other than missing material) should be directed to the corresponding author for the paper.

## APPENDIX A: SENSITIVITY OF SEISMIC DATA TO DISCONTINUITY TOPOGRAPHY IN THE TRANSITION ZONE

The sensitivity of *S*-wave traveltimes on transition zone discontinuity topography $\Delta r$ is given by

$$\delta t_i = -K \sum_{j=1}^{\hat{N}} \Delta r\left(\omega_j\right), \tag{A1}$$

where $\omega_j = (\Theta_j, \Phi_j)$ defines the locations of 'piercing' points at discontinuities in the transition zone for a particular ray, $\hat{N}$ is the number of piercing points for a particular wave and $K$ is given by the following formula (Dziewonski & Gilbert 1976):

$$K = \lim_{e \to 0} \left[ \left( \frac{1}{v^2 (r+e)} - \frac{p^2}{(r+e)^2} \right)^{\frac{1}{2}} - \left( \frac{1}{v^2 (r-e)} - \frac{p^2}{(r-e)^2} \right)^{\frac{1}{2}} \right], \tag{A2}$$

where $v$ is the velocity at a radius $r$ and $p$ is the ray parameter for the corresponding wave. We assumed the PREM velocity jumps on discontinuities in the transition zone (Dziewonski & Anderson 1980).

We use a spherical harmonic expansion to represent discontinuity topography given by

$$\Delta r\ (\omega) = \sum_{l=1}^{L} \sum_{m=-l}^{l} \Delta\, r_l^m\, Y_l^m\,(\omega), \tag{A3}$$

and knowing that $\Delta\, r_l^{-m} = (-1)^m\ \overline{\Delta r_l^m}$ and $Y_l^{-m} = (-1)^m\ \overline{Y_l^m}$ where $\overline{\Delta r_l^m}$ and $\overline{Y_l^m}$ are complex conjugates, eq. (A1) can be rewritten as:

$$\delta t = P_S\, \Delta r, \tag{A4}$$

where

$$\Delta r = \left[(\Delta r)_1^0,\ \mathrm{Re}\,(\Delta r)_1^1,\ \mathrm{Im}\,(\Delta r)_1^1,\ (\Delta r)_2^0,\ \ldots,\ \text{up to } l = L \text{ and } m = L\right], \tag{A5}$$

and

$$P_S = [-K\sum_{j=1}^{\hat{N}} Y_0^0(\omega_j),\ -2K\mathrm{Re}\left(\sum_{j=1}^{\hat{N}} Y_1^1(\omega_j)\right),\ -2K\mathrm{Im}\left(\sum_{j=1}^{\hat{N}} Y_1^1(\omega_j)\right),\ -K\sum_{j=1}^{\hat{N}} Y_2^0(\omega_j),\ \ldots, \text{ up to } l = L \text{ and } m = L] \tag{A6}$$

$l$ and $m$are spherical harmonic degree and order, respectively. $L$ is the maximum degree of spherical harmonic expansion. We used $L = 16$ for $\Delta r$ in this study, which is a conservative choice based on previous studies (e.g. Wei & Shearer 2017) which suggest reduced resolution in the seismic data at higher orders.

To calculate the SdS sensitivity to phase undulations in the transition zone, $P_{\mathrm{SdS}}$, instead of using eq. (A2) we use a term for a bottom-side reflection of a ray (Dziewonski & Gilbert 1976):

$$K = \lim_{e\to 0} 2\left(\frac{1}{v^2(r-e)} - \frac{p^2}{(r-e)^2}\right)^{\frac{1}{2}}. \tag{A7}$$

For example, the $K$-values (eqs A2 and A7) for the 410-km discontinuity are 0.0079 and 0.3520 s km$^{-1}$ for an SS-wave and an S410S-wave if p = 600 s rad$^{-1}$, respectively. Therefore, the sensitivity of the transmitted shear wave data to discontinuity deflections is low while the SdS waves are far more sensitive.

## APPENDIX B: SENSITIVITY OF GEODYNAMIC DATA TO TOPOGRAPHY ON INTERNAL DISCONTINUITIES

An approximation for the lateral density variation, $\delta\rho_b$, due to topographic undulations, $\Delta r$, on an internal discontinuity located at mean radius, $r = r_b$, is given by

$$\delta\rho_b(\Theta,\Phi) = \Delta\rho_b \Delta r(\Theta,\Phi)\,\delta(r - r_b), \tag{B1}$$

where $\Delta\rho_b$ is the density jump across the discontinuity and $\delta(r - r_b)$ is a Dirac delta function.

Expression (B1) is accurate when $\Delta r/r_b \ll 1$. The spherical harmonic coefficient of an arbitrary surface geodynamic observable, $G(\Theta,\Phi)$, can be expressed by the following formula (Forte *et al*. 2015):

$$G_l^m = g_l \int_a^b \left[\widehat{G_l}(r)\left(\widehat{\delta\rho}\right)_l^m(r) + \overline{G_l}(r)\left(\overline{\delta\rho}\right)_l^m(r)\right]dr, \tag{B2}$$

where $G_l^m$ are the harmonic coefficients of the observable, $g_l$ is the corresponding scale factor (Forte *et al*. 2015), $\widehat{G_l}$ is the free-slip kernel, and $\overline{G_l}$ is the no-slip kernel. Based on theory presented in Forte & Peltier (1994), the viscous coupling of plate motions to the flow in the underlying mantle involves a separation of mantle density anomalies $\delta\rho$ into two distinct components: $\widehat{\delta\rho}$ and $\overline{\delta\rho}$ that are modelled with free-slip and no-slip surface boundary conditions, respectively. The density perturbations $\widehat{\delta\rho}$ are obtained using a spectral projection operator $\widehat{P_{ls}^{mt}}(r)$, derived from the tectonic plate geometries (Forte & Peltier 1994), as follows:

$$\left(\widehat{\delta\rho}\right)_l^m(r) = \widehat{P_{ls}^{mt}}(r)\,(\delta\rho)_s^t(r) \text{ (summation over all } s, t \text{ is implied)}, \tag{B3}$$

and

$$\left(\overline{\delta\rho}\right)_l^m(r) = (\delta\rho)_l^m(r) - \left(\widehat{\delta\rho}\right)_l^m(r). \tag{B4}$$

$$G_l^m = \langle g_l \Delta\rho_b \left(\left[\widehat{G_l}(r_b) - \overline{G_l}(r_b)\right]\widehat{P_{ls}^{mt}} + \overline{G_l}(r_b)\,\delta_{ls}^{mt}\right)\rangle\ (\Delta r)_s^t, \tag{B5}$$

where the terms in $\langle\rangle$ determine the geodynamic sensitivity kernel for internal discontinuity topography and

$$\delta_{ls}^{mt} = \begin{cases} 1, & (l,m) = (s,t) \\ 0, & (l,m) \neq (s,t) \end{cases}. \tag{B6}$$